NOAA Technical Memorandum ERL ETL-284

LABORATORY MODELING AND THEORETICAL STUDIES OF WAVE PROCESSES IN THE OCEAN

Part 2: First Stage Results

L.A. Ostrovsky, Editor

Environmental Technology Laboratory
Boulder, Colorado
November 1997

noaa NATIONAL OCEANIC AND ATMOSPHERIC ADMINISTRATION / Environmental Research Laboratories

NOAA Technical Memorandum ERL ETL-284

LABORATORY MODELING AND THEORETICAL STUDIES OF WAVE PROCESSES IN THE OCEAN

Part 2: First Stage Results

L.A. Ostrovsky, Editor

Environmental Technology Laboratory
Boulder, Colorado
November 1997

NOTICE

Mention of a commercial company or product does not constitute an endorsement by the NOAA Environmental Research Laboratories. Use of information from this publication concerning proprietary products or the test of such products for publicity or advertising purposes is not authorized.

The memorandum presents the results obtained from the first stage of the work of the Institute of Applied Physics (IAP) of the Russian Academy of Sciences, performed in the framework of an Agreement between IAP and the National Oceanic and Atmospheric Administration (NOAA) Environmental Technology Laboratory (ETL). The work was supported by the joint NOAA/DOD Advanced Sensor Applications Program (ASAP).

Head of the Project: V.I. Talanov
Program Coordinator: L.A. Ostrovsky
Authors: V.V. Bakhanov, K.A. Gorshkov, E.M. Gromov, O.N. Kemarskaya, L.A. Ostrovsky, V.V. Papko, V.I. Talanov, Yu. I. Troitskaya, S. N. Reznik, I.A. Soustova
Translator: N.V. Rudik

For sale by the National Technical Information Service, 5285 Port Royal Road
Springfield, VA 22061

Contents

Laboratory Modeling and Theoretical Studies of Wave Processes in the Ocean

Part 2: First Stage Results

Edited by L. A. Ostrovsky

Abstract

The results of theoretical studies and laboratory modeling of waves and vortices in the upper ocean are presented. In particular, structure of surface wave contrasts due to the inhomogeneous flow around a dipole-type obstacle, wave drag in a stratified fluid in the presence of a critical layer, and vortex pair motion in the presence of a pycnocline are calculated. The experiments deal with different aspects of propagation of strong (nonlinear) surface gravity waves: self-steepening of wave packets and amplitude dependence of phase velocities in traveling and standing (counterpropagating) waves. These results are believed to be important to better understand the processes in the upper ocean to be observed by remote sensing methods.

1 Introduction

In the previous memorandum [1], after a description of the unique laboratory facilities of IAP, we outlined the main problems to be solved in the framework of a planned study of upper ocean dynamics. This and the following memoranda will describe the results of these studies. They are divided into theoretical and experimental chapters and cover a rather wide range of problems. In this part we consider first several complicated theoretical problems important for understanding the upper ocean processes. They include manifestations of internal inhomogeneities such as bottom features and

submerged bodies due to subsurface current variations, internal wave radiation due to the internal inhomogeneities, and vortex pair dynamics under the action of density stratification. The experimental section describes observations of nonlinear gravity wave train propagation in a large tank and a detailed study of the dependence of phase velocity of interacting nonlinear gravity waves on their amplitudes.

2 Theoretical studies

2.1 Manifestations of inhomogeneous flows on the ocean surface

The most promising method for investigating spatial inhomogeneities of the ocean is remote sensing from air/space carriers. This is a complicated problem, since remote-sensing facilities provide information primarily on the ocean surface. Thus, of primary interest is the transformation of surface waves under the action of underwater processes. This section deals with variability of surface waves running counter to the flow at a weak localized perturbation of the flow. This situation exists, for example, in the case of the streamlining of different submarine inhomogeneities. In particular, the assigned problem is of interest for determining the bottom topography and other subsurface features from space. It will be shown that even relatively weak perturbations of the flow may essentially change the spatial distribution of energy for surface wind waves if their group velocity is close to the speed of the flow.

2.1.1 Basic equations

Analysis of the transformation of quasi-monochromatic surface waves is based on the equation for the complex amplitude of the surface wave a considered in Part 1 [1]:

$$\begin{aligned} \frac{\partial a}{\partial \widetilde{t}} = 2i\,(-\Delta)^{1/4}\,a + (1-\beta_x)\,\frac{\partial a}{\partial \widetilde{x}} - \beta_y \frac{\partial a}{\partial \widetilde{y}} + \\ \left((-1+\beta_x)\,\widetilde{k}_{x0} + \beta_y\,\widetilde{k}_{y0} - \widetilde{\omega}\right) a, \end{aligned} \tag{1}$$

where the operator $(-\Delta)^{1/4}$ is introduced as follows:

$$(-\Delta J)^{1/4}\left(\tilde{x},\tilde{y}\right)=\frac{1}{2\pi}\int\exp\left(-i\left(k_x^{/}\,\tilde{x}+k_y^{/}\,\tilde{y}\right)\right)$$
$$\left[\left(\tilde{k}_{x0}-k_x^{/}\right)^2+\left(\tilde{k}_{y0}-k_y^{/}\right)^2\right]^{1/4}\tilde{J}\left(k_x^{/},k_x^{/}\right)dk_x^{/}dk_y^{/},$$

while $\tilde{J}\left(k_x^{/},k_x^{/}\right)$ is the Fourier transformation of the function J

$$\tilde{J}\left(k_x^{/},k_x^{/}\right)=\frac{1}{2\pi}\int\exp\left(-i\left(k_x^{/}\,\tilde{x}+k_y^{/}\,\tilde{y}\right)\right)J\left(\tilde{x},\tilde{y}\right)d\,\tilde{x}\,d\,\tilde{y}\,.$$

In equation (1) the dimensionless variables $\tilde{t}=k_*Vt$, $\tilde{x}=k_*x$, $\tilde{y}=k_*y$ are used, where V is the velocity of unperturbed flow directed counter to the axis x, $k_*=g/4V^2$ is the wave vector of the surface wave, the group velocity of which equals V. The parameters of an unperturbed surface wave are $\tilde{\omega}_0=\omega_0/k_*V$, $\tilde{k}_{x0}=k_{x0}/k_*$, $\tilde{k}_{y0}=k_{y0}/k_*$. The field of the flow perturbation on the surface $\overrightarrow{u}\,(x,y)$ is assigned by the dipole field at a depth h:

$$\beta_x=u_x/V=c\frac{2\,\tilde{x}^2-\tilde{y}^2-\tilde{h}^2}{\left(\tilde{x}^2+\tilde{y}^2+\tilde{h}^2\right)^{5/2}}$$

and

$$\beta_y=u_y/V=3c\frac{\tilde{x}\tilde{y}-\tilde{h}^2}{\left(\tilde{x}^2+\tilde{y}^2+\tilde{h}^2\right)^{5/2}},$$

where c is the dipole power, $\tilde{h}=hk_*$. The characteristic scales of the flow inhomogeneity are assumed to be much larger than the length of scattered waves.

In the absence of flow perturbations ($\beta_x=\beta_y=0$) the function $a\left(\tilde{x},\tilde{y},\tilde{t}\right)$ is a harmonic one, and we have a plane wave of the frequency ω_0 with the wave vector $\overrightarrow{k}_0$ over the entire space. Further, we shall assume its amplitude a_0 to be equal to 1.

Let us consider temporal evolution of the initially homogeneous wave field when a perturbation $\overrightarrow{u}$ appears at some instant of time $t=0$. Then a spatial

pattern of wave scattering develops and spreads with time; in the vicinity of the scattering source it tends to a stationary pattern. The wave field perturbations caused by the inhomogeneous current will spread to infinity. There exists no steady-state spatial distribution of the perturbations on the whole surface; however, in the course of the field evolution, a quasi-stationary pattern is formed around the area of current localization.

Equation (1) was numerically solved by using a method of characteristics in a square of sizes 1024 x 1024, in dimensionless units $\tilde{x}$ and $\tilde{y}$ (the grid had 256 x 256 points).

The parameter of the problem determining the picture of the wave field variation for the assigned functions β_x and β_y is the wave vector of the incident wave $\overrightarrow{k}_0$. First we consider the case $k_{y0} = 0$ symmetric with respect to the x axis. In the absence of flow perturbations $\beta_x = \beta_y = 0$ at $\tilde{k}_{x0} < 1$, the group velocity of the wave is $V_{gx}^{(0)} = \frac{\partial \omega}{\partial k_x}\Big|_{k_x = k_{x0}} > 0$. In this case a short wave packet would move in the direction of the x axis and counter to the speed of the main flow. At $\tilde{k}_{x0} < 1$ the situation is reversed. Although in the latter case the wave vector of an incident wave is also directed counter to the flow (along the x axis), nevertheless $V_{gx}^{(0)} < 0$. This is because the group velocity of the wave with respect to water is less than the velocity of the main current V. Therefore, in a laboratory reference system, the wave packet is drifted by the current, and the group velocity is negative. When the incident wave propagates at an angle to the flow ($k_{y0} \neq 0$), there is a component of the group velocity $V_{gy}^{(0)}$, and its sign coincides with k_{y0}. In this case the spatially limited wave packet running in the same direction with the current or counter to it will also move across the current.

Since at scattering by a weak, inhomogeneous current the value of the wave vector variation is small, and the main role in the transformation of the surface wave field is played by the forward scattering, one can expect that the main variations of the wave field at $\tilde{k}_{x0} > 1$ will occur in the region located downstream from the dipole ($x < 0$). Accordingly, at $\tilde{k}_{x0} < 1$, the variations will primarily occur at $x > 0$. At $\tilde{k}_{y0} > 0$, the variations will take place mainly for $y > 0$, and vice versa at $\tilde{k}_{y0} < 0$ for $y < 0$.

2.1.2 Calculation results

The theoretical results discussed above were supported by numerical calculations. First we consider the case $\tilde{k}_{x0}= 1$, $\tilde{k}_{y0}= 0$. Variations of the value $|a|$ calculated for the parameter values $c = 2$, $\tilde{h}= 10$ are given in Figs. 1a and 1b. The first figure corresponds to the time $\tilde{t}= 900$, the second one to $\tilde{t}= 1500$. The main qualitative peculiarity of the obtained picture is the distinctly pronounced cross-shaped figure in the plane (x, y). The inclination angle of the corresponding lines to the x axis is of the order of $50 - 60°$. As seen from Figs. 1a and 1b, the space occupied by this structure increases with time. Simultaneously, the variation of the perturbation structure for the value $|a|$ in the vicinity of the scattering current ceases to depend on time, so that in this region the picture is close to a stationary one.

In the case of an essential difference of $\tilde{k}_{x0}$ from 1 (at $\tilde{k}_{y0}= 0$), the perturbation picture is slightly different. The calculation results for $\tilde{k}_{x0}=$ 1.2 and the time $\tilde{t} = 1500$ are shown in Fig. 1c. In accordance with the considerations presented in the previous subsection, the perturbations here are mainly concentrated in the region $x < 0$.

The calculation results for the cases when $\tilde{k}_{y0}\neq 0$ and the unperturbed wave has a component of group velocity along the y axis are presented in Figs. 1d and 1e. Figure 1d corresponds to the case $\tilde{k}_{x0}= 1$, $\tilde{k}_{y0}= 0.2$, $\tilde{t}= 1500$, while Fig. 1e to $\tilde{k}_{x0}= 0.8$, $\tilde{k}_{y0}= 0.2$, $\tilde{t}= 1500$. As expected, the wave field perturbations are localized at such values of the parameters in the region $y > 0$. In these cases the perturbations are concentrated in some rather narrow sector of angles. The Figure 1d characterizes the dependence of qualitative properties of the wave field perturbations in the inhomogeneous stream induced by a dipole on the conditions of the wave incidence.

To provide a quantitative characteristic of the perturbations, Fig. 2 displays the time dependences of the maximum $|a|_{\max}$ and minimum $|a|_{\min}$ values of the modulus of the wave field amplitude $|a|$ over the entire region of the calculations. The curves are shown for various values of the parameters $\tilde{k}_{x0}$, $\tilde{k}_{y0}$, and $\tilde{h}$ at fixed $c = 2$. According to Fig. 2, maximum variations $|a|$ are observed at $\tilde{k}_{x0}= 1$, $\tilde{k}_{y0}= 0$. The value $\delta a = |a|_{\max} - |a|_{\min}$ at $\tilde{h}= 10$, $\tilde{t}= 3000$ achieves 0.23. For a mismatch of the wave vector of the unperturbed surface

wave from the synchronous value by about 20%, the increase of δa ceases at $\tilde{t}$= 300 and achieves the level 0.06. The calculations for the case of large $\tilde{h}$ made at $\tilde{k}_{x0}$= 1, $\tilde{k}_{y0}$= 0 demonstrate that the picture of the wave field perturbations has qualitatively the same form as at $\tilde{h}$= 10. However, the velocity of the perturbation gain and their maximum value decrease with an increase of the depth $\tilde{h}$.

2.1.3 Analysis of computation results

The results obtained will be treated using the analysis of the dispersion equation for surface waves in the flow. We employ the representation of the dispersion ratio involving isofrequencies, the lines of constant $\tilde{\omega}$ on the plane (k_x, k_y). Due to the relation $\vec{V}_g = \frac{\partial \omega}{\partial \vec{k}}$ the perpendicular to the isofrequency indicates the direction of the group velocity of the wave with the given frequency and the wave vector in the coordinate space. The isofrequencies are illustrated in Fig. 3 for the case $\beta = 0$ and different frequencies and propagation directions of the incident wave. Arrows show the direction of the group velocities for various values of the wave vector $\vec{\tilde{k}}$. There are two families of isofrequencies in this case: those crossing the $\tilde{k}_x$ axis correspond to the value $\tilde{\omega}$< 1, while the isofrequencies crossing the $\tilde{k}_y$ axis correspond to $\tilde{\omega}$> 1. Since in the process of the wave scattering at an inhomogeneous but stationary current its frequency $\tilde{\omega}$ does not vary in the laboratory reference system, the scattered waves will have the same isofrequency as the incident wave but different values of $\vec{\tilde{k}}$. Therefore, the isofrequencies can be employed when determining the character of the scattered wave field.

Curves marked "1" in Fig. 3 correspond to the case $\tilde{k}_{x0}$= 1, $\tilde{k}_{y0}$= 0, while point a of this curve refers to the incident wave. Scattered waves will have different values of the wave vector; in particular, the component $\tilde{k}_{y0}$ appears. The characteristic variations of the wave vector $\Delta \vec{\tilde{k}}$ at scattering of the incident wave depend on the scale of the stream inhomogeneity and on the value β. In this case scattered waves will diverge from the region of the inhomogeneous flow in the directions normal to curves 1, i.e., $\approx 55°$ to the x axis.

The results of the calculations given in Fig. 1c, $\widetilde{\omega} < 1$. This case is demonstrated by curves 2 in Fig. 3, point **b** of which corresponds to the incident wave. The variations of the wave vector $\left|\Delta \overrightarrow{\widetilde{k}}\right|$ prove to be less than $2\left(\widetilde{k}_{x0} - 1\right)$; therefore, the scattered waves have the wave vectors that belong only to the right branch of the isofrequency. Accordingly, the wave field perturbations occur only in the space region located downstream from the dipole, at $x < 0$.

In the case shown in Fig. 1d when the incident wave has a component of the group velocity across the main stream, the value $\widetilde{\omega}$ is more than unity. This case corresponds to curve 3 in Fig. 3, while point **c** of this curve indicates the wave vector of the incident wave. The relation between the values $\widetilde{k}_{y0}$ and $\left|\Delta \overrightarrow{\widetilde{k}}\right|$ in this case is such that the wave vectors of the scattered waves are concentrated in the vicinity of point **c**. Hence, the wave field perturbations occur at $y > 0$, and no pronounced curves are observed in the spatial picture of the wave field. The situation, the calculation results for which are depicted in Fig. 1e, also corresponds to the value $\widetilde{\omega} > 1$. Curve 4 in Fig. 3 also refers to it, while point **d** of this curve corresponds to the incident wave. It is evident that in this case the left part of the upper branch of the isofrequency proves to be singled out, which ensures the wave field variability in a narrow sector of angles in Fig. 1e.

2.1.4 Conclusions

The above investigation shows that under some conditions an inhomogeneous current created by streamlining of a submarine obstacle may cause essential variations in the wave field of surface waves even if the perturbation of the stream velocity on the surface is small. According to our calculations, for the characteristic flow velocities $V = 1$ m/s, the maximum value of current perturbations amounts to 0.2 cm/s. The maximal variations occur in the picture of surface waves of lengths 2.5 m; relative variations of the modulus of the quasi-monochromatic wave amplitude may achieve 0.23. In this case, the spatial dimensions of the region where the wave transformation is essential, by far (10 times) exceed the scales of the inhomogeneous current

itself. The picture of the wave transformation is anisotropic; in particular, the directions are singled out where the main variations of the surface wave field are concentrated.

The results of this theoretical investigation will be verified later in laboratory experiments.

2.2 Wave drag in a stratified shear flow with a critical layer

The wave drag force acting on a body submerged in a stratified fluid is a significant practical problem. It has recently been studied in detail for bodies moving in a fluid at rest [2, 3], whereas the influence of the shear flow is scantily studied. Of special interest here is the case when the velocity of the body motion coincides with the flow velocity at some level. This situation can be typical of slowly moving, submerged apparata. Then a critical layer (CL) forms in the vicinity of this level for the body-generated waves the velocity of which is equal to that of the body. A similar problem regarding the wave drag of a two-dimensional, localized, bottom inhomogeneity in the stratified shear flow changing its direction at some level, in the vicinity of which CL formed, was considered in [4]. It has been demonstrated that the presence of CL results in essential variation of the wave drag (including its strong increase for some parameters of the flow) compared to the case of homogeneous flow streaming.

Here we will consider new effects that appear when the obstacle is placed at some depth over the solid bottom in a stratified shear flow, and it moves with a velocity equal to that of the flow at some other depth. At this stage two-dimensional case will be studied for simplicity. The obstacle is modeled by a mass source. The main qualitative peculiarities of the wave drag force under these conditions are discussed.

2.2.1 Formulation of the problem

Let us consider the shear flow of a density-stratified fluid over a solid bottom. This fluid is characterized by the constant buoyancy frequency $N = \left(-\frac{g}{\rho_0}\frac{d\rho_0}{dz}\right)^{1/2}$ and the constant velocity shear U_{0z}. The fluid density is $\rho_0(z)$, where z is the vertical coordinate, and the vertical axis is directed down-

ward. We assume that the flow is dynamically stable, i.e., the Miles criterion for the gradient Richardson number $Ri = \frac{N^2}{U_{0z}^2} - Ri > 1/4$ [5, 6] is fulfilled everywhere. A cylindrical body moves in the flow at a distance d from the surface, its velocity V_0 being coincident with the flow velocity at some level. CL forms in the vicinity of this level for the body-produced waves that have the phase velocity V_0.

Now we consider a coordinate frame moving with the velocity V_0. The geometry of the problem is plotted in Fig. 4. The flow velocity in CL is zero. Then the velocity profile is $u_0 = U_{0z}z$, and the surface coordinate is $z_0 = (U_0 - V_0)/U_{0z}$, where U_0 is the flow velocity on the surface in the rest coordinate frame, the body coordinate is $h = z_0 - d$. In this case $h > 0$, if the body is under CL, and $h < 0$, if the body is over it. We shall model the submerged body using the localized mass source $m(x, z)$, where x is the horizontal coordinate measured down the flow, and $x = 0$ corresponds to the center of the body. Due to the assumption that the amplitude of the internal waves generated by a body is small enough, we employ a linear approximation for their treatment. Since these waves are stationary in the considered coordinate system, the corresponding set of hydrodynamic equations has the form

$$u_0\frac{\partial u_1}{\partial x} + w_1\frac{dU_0}{dz} + \frac{1}{\rho_0}\frac{\partial p_1}{\partial x} = 0,$$

$$u_0\frac{\partial w_1}{\partial x} + \frac{1}{\rho_0}\frac{\partial p_1}{\partial z} + \frac{\rho_1 g}{\rho_0} = 0,$$

$$u_0\frac{\partial \rho_1}{\partial x} + w_1\frac{d\rho_0}{dz} = 0,$$

$$\frac{\partial u_1}{\partial x} + \frac{\partial w_1}{\partial z} = m(x, z). \qquad (2)$$

Here u_1, w_1, p_1, ρ_1 are perturbations of the horizontal and vertical velocities, pressure, and density. The characteristic value of the function $m(x, z)$ - m_0 is proportional to the cross-section area D_0 and to its streaming velocity [7]. All perturbations of the hydrodynamic fields are linear in m_0. The boundary conditions for set (1) are the no-leaking condition on the surface $z = z_0$:

$$w_1 \mid_{z=z_0} = 0, \tag{3}$$

and the perturbation decrease at large distances from it:

$$w_1 \mid_{z \to -\infty} = 0. \tag{4}$$

The set (2) is valid outside the CL vicinity where its solutions have singularities. Additional factors should also be taken into account in these regions: the viscosity and diffusion [8], the nonlinearity [9] and the unsteady state [10] of wave perturbations. To remove the singularities while considering wave perturbations outside the CL vicinity, we shall employ the known Lin rule [11] valid in the case when wave perturbations are linear.

2.2.2 Forces affecting a body submerged in a stratified shear flow

Taking into account the hydrodynamic equations and the equation for the wave energy gives the expression for the force acting on the length unit of a cylindrical body submerged in a stratified shear flow in the case when CL exists for the waves generated by the body in the following form:

$$f_x = \rho_0 \langle u_1 w_1 \rangle \Big|_{z=0} - \rho_0 \int_0^{z_0} \frac{u_{0z}}{u_0} \left\langle w_1 \int_{-\infty}^{x} m dx_1 \right\rangle, \tag{5}$$

where $\langle ... \rangle = \int_{-\infty}^{\infty} dx$.

The first term in (5),

$$D_1 = \rho_0 \langle u_1 w_1 \rangle \Big|_{z=0}, \tag{6}$$

determines the drag force acting on the body due to the generation of waves absorbed in CL, i.e. the wave loss. The second term

$$D_2 = \rho_0 \int_0^{z_0} \frac{u_{0z}}{u_0} \left\langle w_1 \int_{-\infty}^{x} m dx_1 \right\rangle, \tag{7}$$

arises because due to wave radiation, the vertical velocity component appears in the place of the body location, which causes the horizontal force in the

vortex flow (the Magnus effect). This is a "lift force" by its nature, which depends on the vector product of the velocity and vorticity, and its horizontal component is determined by the vertical component of the wave perturbation of the velocity w_1. The force affecting the circular cylinder in a shear flow taking into account this "lift force" is calculated in [13]. In the absence of the velocity shift ($u_{0z} = 0$) this force is zero, while the force acting on the body is determined only by the energy loss due to wave radiation. The estimates of this "lift force" are given below.

2.2.3 Wave drag

First we calculate the force affecting the body due to the radiation loss D_1 determined by formula (6). By using the Fourier representation for hydrodynamic fields, one can easily obtain that

$$D_1 = 4\pi\rho_0 \int_0^\infty Im\left(\frac{W^*(k,z)W_z(k,z)}{k}\right) dk \Bigg| \; z = 0, \tag{8}$$

where

$$W(k,z) = \int_{-\infty}^{\infty} w_1(x,z)e^{-i\kappa x}dx$$

is the Fourier image of the vertical velocity. $W(k,z)$ satisfies the equation

$$\frac{d^2W(k,z)}{dz^2} + W(k,z)\left(\frac{Ri}{z^2} - k^2\right) = \frac{M(k,z)}{z} + \frac{dM(k,z)}{dz}. \tag{9}$$

with the boundary conditions

$$W(z,k)\,|_{z=z_0} = 0$$

and

$$W(z,k)\,|_{z\to-\infty} = 0. \tag{10}$$

Here $M(k,z) = \int_{-\infty}^{\infty} m(x,z)e^{-i\kappa x}dx$ is the Fourier transformation of the mass source. We shall assume that the source is localized around the level

$z = h$, and its characteristic vertical size b is small compared to the length of the radiated wave (a "boardlike" source). Hence when calculating wave fields at a large distance from the source, one can assume that

$$m(x,z) = Uf\left(\frac{x}{a}\right)\delta(z-h)\frac{b}{a}.$$

Here $U = U_{0z}h$ is the flow velocity at the level $z = h$, $f(x/a)$ is the dimensionless function, and a is the characteristic horizontal size of the source. The spectral representation of the source $m(x,z)$ has the form

$$M(k,z) = UbF(ka)\delta(z-h), \tag{11}$$

where $aF(ka)$ is the spectrum of the function $f(x/a)$, and F is the dimensionless function. We shall suppose that $F(0) = 0$; this corresponds to the fact that the sources and sinks will compensate each other. In this case the expression for the force determined by the wave loss can, by analogy with [4], be represented as

$$D_1 = 4\pi\rho_0 ab^2N^2G_1\left(Ri, Fr, \frac{z_0}{h}\right). \tag{12}$$

Here $Fr = U/(aN)$ is the Froude number, and

$$G_1\left(Ri, Fr, \frac{z_0}{h}\right) = \frac{1}{Fr}\int_0^\infty \left|\Phi\left(\frac{\kappa}{Fr}\right)\right|^2 f\left(\kappa, Ri, \frac{z_0}{h}\right) d\kappa. \tag{13}$$

Integration is carried out with respect to the dimensionless wave number $\kappa = kU/N$. The integrand in (13) is the product of the dimensionless spectrum modulus of the source

$$\Phi\left(\kappa/Fr\right) = F(ka)/ka = FrF(\kappa/Fr)/\kappa$$

and the transfer function f. The function f is yielded by the solution of (9) with the boundary conditions (10). The procedure is analogous to that given in [4] and is described in [12]. It is noteworthy that, as distinct from the formulas obtained in [4], the transfer function f depends on the additional parameter z_0/h. For $z_0 = h$, f transforms into the expression for the transfer function obtained in [4], while (13) transforms into the formula for the wave

drag of the source in the form of the surface elevation if $F(ka) = k\xi(ka)/b$, where $\xi(ka)$ is the spectrum of the surface elevation.

As in [4], the function f has the sense of the momentum flux withdrawn from the source by the k-th harmonic of the unit amplitude. It should be taken into account that at some depths above the surface $d(k)$, the incident and reflected waves with a definite wave number k and equal amplitudes are added in the opposite phase. If the source is located at the height $d = d(k)$, the corresponding k-th harmonic is not generated. As a result, the value of the transfer function proves to be zero. As an illustration, the dependences of the transfer function on κ for various Ri and $d/z_0, h > 0$ are presented in Fig. 5 (a-d). It is seen that the number of zeros of the function f grows at fixed Ri with increase of d/z_0 and at fixed d/z_0 with increase of Ri.

Using expression (13), we consider now the dependence of the wave losses determined by the function G_1 on the parameters of the flow and the source for the case when the source spectrum has the form

$$\Phi(\frac{\kappa}{Fr}) = \frac{1}{2}e^{-\frac{|\kappa|}{Fr}}.$$

Taking into account the designations introduced in section 1, one can see that $Fr = d/a(|v - 1/\sqrt{Ri}|)$, $z_0/h = \sqrt{Ri}/(\sqrt{Ri} - 1/v)$, where $v = (U_0 - V_0)/Nd$.

Therefore, $G_1 = G_1(Fr, a/d, Ri)$ is the function of the Froude number determined by means of the source velocity with respect to the flow, the relative size of the source a/d, and the Richardson number. Figure 6a deals with a family of the dependences G_1 on (Fr) in the case when CL is higher than the source $(h > 0)$ at $a/d = 0.1$. The curves differ by the value of Ri; $Ri = \infty$ corresponds to the flow with a homogeneous velocity profile. Note that the variation of Fr at constant Ri and a/d can be provided by variation of the body speed in a fixed flow at a fixed height above the surface. It is seen that at large Ri the dependences have the oscillating character, the number of oscillations growing with increase of Ri. The value of wave losses in a shear flow essentially differs from its value in a homogeneous flow. In this case at Fr close to 1 (close to the maximum of the wave drag) the value of the radiation loss in the shear flow essentially exceeds its value in a homogeneous flow. The cause of this phenomenon is associated with the expansion of the generated wave spectrum in the shear flow; it is thoroughly discussed in [4].

The dependences $G_1(Fr)$ in the case when CL is lower than the source $(h < 0)$ are shown in Fig. 6b. These curves are determined within the interval

$0 < Fr < \frac{d}{a\sqrt{Ri}}$. At $Fr > \frac{d}{a\sqrt{Ri}}$ CL is absent, and the waveguide for internal waves arises on the linear velocity profile. Then the wave drag is determined by the sum of contributions of discrete natural waves of the waveguide. This case will not be considered here.

The dependences G_1 on a/d at $Fr = 1$ for various Ri are presented in Fig. 6(c,d). At small a/d when a source is located at a large distance from the bottom compared to its size, $G_1$is almost constant. With increase of a/d, $G_1(Fr)$ varies and tends to some fixed value at $a/d \to \infty$ corresponding to the wave drag of the surface elevation.

Let us now give estimates of the "lift force" D_2 (see (7)) which affects a body modeled by a mass source. We shall assume as before that the characteristic vertical size of the source b is small compared to the radiated wave length. However, when considering wave fields at large distances from the source, it could be represented as δ-function (11), but now when integrating over the source region in (7) one should employ the source model having a small but finite size in the vertical direction. By analogy with (11) we represent $m(x,z)$ and $M(k,z)$ as

$$m(x,z) = Uf(x/a)q\left(|z-h|/b\right)$$

and

$$M(k,z) = UaF(ka)q\left(|z-h|/b\right). \tag{14}$$

We move on to the spectral representation in the expression for the "lift force." After some transformations we have, at $h > 0$,

$$D_2 = 4\pi\rho_0 N^2 ab^2 G_2\left(Ri, Fr, \frac{z_0}{h}\right), \tag{15}$$

where

$$G_2\left(Ri, Fr, \frac{z_0}{h}\right) = \frac{1}{Fr}\int_0^\infty \left|\Phi\left(\frac{\kappa}{Fr}\right)\right|^2 f_2\left(\kappa, Ri, \frac{z_0}{h}\right) dk.$$

It is seen from Figs. 6, (c,d) that at large Ri the "lift force" is small compared to the wave loss, at Ri of the order of 1 they are comparable, and at Ri close to $1/4$ at some Fr the "lift force" can exceed the force due to radiation loss. It is seen from (5) that the total "wave" force acting on the body is

$$D = D_1 - D_2,$$

and it can be expected that in the corresponding regions of the parameters, the force D will fall abruptly or even its sign will be changed.

It should be noted that the qualitative effect of the horizontal component of the "lift force" also exists at streamlining of a real body (not a model source). This is because the wave generation leads to the flow asymmetry with respect to the horizontal plane passing through the body center (a vertical velocity component occurs). In a flow with vorticity, this causes the appearance of the horizontal force (the Magnus effect). But for correct calculation of the value of this force, of special importance is the proper choice of the source, which can be based on the experiment.

2.2.4 Conclusions

Waves radiated by a submerged body moving with a velocity comparable with those of ocean flows can have critical layers (CL) where the flow velocities coincide with the body velocity. The singularities associated with CL strongly affect the wave drag force acting on the submerged bodies. It can be seen from Fig. 6a, where the sign ∞ marks the dependence of the wave drag force on the Froude number Fr in the flow with the homogeneous velocity profile and the numbers near the other curves denote the values of the Richardson number Ri in the shear flows. For $Fr \simeq 1$ radiation force in the shear flow is evidently much larger than this value in the uniform flow. At the same time, one can see that for $Ri \leq 1$ and $Fr \sim 1$, the value of the horizontal component of the "lift force" is compared with the wave force caused by the radiation losses. As a result, the full force acting on the body, which is equal to the difference of these forces, appears to be much smaller than each of these components (although still larger than the force acting on a body in a uniform flow (see Fig. 6a)).

It should be mentioned that this result is the consequence of the model in use, in which the velocity profile is supposed to be linear and the obstacle generating waves is placed into the flow with the nonzero vorticity. For the flow with the velocity profile approximated by the hyperbolic tangent more typical of the ocean, the effect of the radiation loss enhancement due to the

CL would also be present, but the horizontal component of the "lift force" would be much smaller than that in the vortex flow.

Finally we note that the "lift force" itself does not contribute to the radiation losses, because the full "lift force" is perpendicular to the full velocity of the moving obstacle.

2.3 Dynamics of vortices in a stratified fluid

It is known that hydrodynamic vortices can serve as effective wave sources in stratified fluids [14]. Such vortex sources exist in the form of thermics in the stratified atmosphere and in the ocean, may be created by moving objects, and may be generated by wave makers under laboratory conditions [15]. Different aspects of internal and surface wave generation by such vortex sources have been considered in a number of papers. Thus, Ref. [16] deals with the results of laboratory observation and numerical simulation of internal wave (IW) generation by vortex pairs moving in the vertical direction around the equilibrium horizon. The IW generation by artificial thermal sources (under laboratory conditions) was considered in a paper [17]. Various theoretical aspects of this problem for homogeneous fluids are discussed in different books on fluid mechanics, including the classical monographs by Lamb [18] and Batchelor [19].

As regards the stratified fluid, mostly numerical results are available. For example, computations based on the contour dynamics method [20] have demonstrated some nontrivial peculiarities in the process of vortex interaction associated, for example, with formation of a vortex sheet [21]. A model was suggested by Saffman [21], according to which, in a smoothly stratified fluid, at the first stage a vortex pair may oscillate with a buoyancy frequency, while the experiments made by Hill [22] show that at later stages the pair is destroyed. Few papers deal with the interaction of a vortex pair with a sharp density interface (see, e.g., [23]).

Analytical results on the dynamics of vortices in a stratified liquid are practically unavailable, except for the extreme cases of the dynamics of point vortices in the presence of a hard or free boundary ([24], [15]). At the same time, of real practical interest for the ocean are the situations when the fluid density variations are small as it always occurs, e.g., for the oceanic thermocline. Those are the problems most closely relevant to the dynamics of the upper ocean considered here.

Here an analytical description is given for the motion of vortices and vortex pairs interacting with each other and with the vorticity generated by density variations. At this stage, the gravity force is neglected, which is justified for large enough Froude numbers of the motion. The method of solution is somewhat similar to the perturbation theory known to be effective for localized, nonlinear waves-solitons, which can be treated as whole entities in the first approximation and can radiate in higher-order approximations (e. g.,[25]). We consider the motion of each vortex as a whole in the first approximation, which suggests that the perturbations are small enough, although they may considerably affect the vortex motion during an extended time interval. The applicability of such a theory is, in general, less universal for vortices than for solitons because the latter are characterized by a finite number of parameters (velocity, amplitude, etc.) while the formers have a less rigid structure [26]. Nonetheless, as it will be shown below, there exist rather typical situations when a vortex can move as a whole for a long enough time under the action of a perturbation, and otherwise, the method used can describe at least the first stage of destroying the vortex.

Here a few basic examples are presented including the motion of a finite-radii vortex pair in the presence of a pycnocline considered as an interface of two media with slightly different densities. We shall not describe the analytical technique in detail but will restrict ourselves to a brief formulation of the main idea of the method.

2.3.1 The idea of the theory

We consider the evolution of plane localized vortex formations affected by perturbations, and proceed from the so-called vortex equation (16),

$$\frac{\partial}{\partial t}\Delta\psi + I(\psi\Delta\psi) = \epsilon R, \tag{16}$$

where $\psi(\mathbf{r}, t)$ is the stream function of a two-dimensional flow ($v_x = \partial\psi/\partial y, v_y = -\partial\psi/\partial x$); $I(u, v)$ is the Jacobian; R is a functional describing perturbations; $\epsilon \ll 1$ is the small parameter characterizing the perturbation. The solution of (16) is constructed as a series

$$\psi = \psi^{(0)} + \epsilon\psi^{(1)} + \dots$$

with a known solution $\psi^{(0)}$ corresponding to a localized vortex formation satisfying the equation (16) for $\epsilon = 0$. The solution of the linearized equation (16) for $\psi^{(1)}$ with $\epsilon \neq 0$, generally contains two groups of eigenfunctions corresponding to the discrete and continuous spectra of modes. Note that only the first (translational) mode of vortex perturbation is responsible for displacement of a single vortex as a whole under the action of perturbation, and its secular growth can be prevented by taking this motion into account. The behavior of other modes depends on their possible resonance with the perturbation R. As a result, the vortices can either move as a whole or be destroyed by the perturbation. The nonbreaking evolution of a vortex is possible only in the absence of such resonances. Examples of adiabatic and breaking evolutions of vortices are outlined below.

2.3.2 Interaction of vortices in a homogeneous fluid

First, we illustrate the results of the theory for the known problem of single vortex motion in a potential field of an another vortex in a homogeneous fluid (Fig. 7). We shall describe the first vortex; however, the expression for the second one is quite similar. In this case, outside the first vortex, $\psi_1^{(0)} = \omega a^2 \ln(r/R)$, ($a$ is the vortex radius, ω is the rotation frequency, r_{12} is a constant that is taken here to equal the distance between the vortex centers, $r_{12} >> a$; the polar coordinates are used here), and the perturbation due to the second vortex is small. It can be shown that modes of continuous spectrum are absent in the solution for $\psi_1^{(1)}$, and the discrete-spectrum modes can be easily found. In particular, for the first (translational) mode the following secularly growing solution occurs:

$$\psi_1^{(1)} = t\frac{\omega_1\omega_2}{r_{12}}a^2 f_1(r)\exp i(\varphi - \varphi_{12}), \tag{17}$$

where $f_1(r) = \frac{\partial\Psi_0}{\partial r}$ is the eigenmode of the first azimuthal harmonic, φ is the polar angle, and φ_{12} characterizes the direction of the vector connecting the vortex centers.

The divergence in time must be compensated by introducing time-dependent coordinates of vortex centers in the generating solution $\Psi_1^{(0)}[x - x_1(t), y - y_1(t)]$. The conditions of finiteness of the corresponding perturbations (compatibility conditions) lead here to the known equations for the motion of a point vortex pair:

$$\dot{x}_{1,2} = \omega_{2,1} a_{21}^2 \frac{\sin\varphi_{12}}{r_{12}}$$

$$\dot{y}_{1,2} = \omega_{2,1} a_{21}^2 \frac{\cos\varphi_{12}}{r_{12}}. \tag{18}$$

This can be considered as a test for the theory used here. At the same time, it is possible to obtain an equation for higher-order approximations describing small deformations of the vortex boundary due to the finiteness of their radii. It may be shown that these perturbations remain finite so that the vortices are never destroyed.

2.3.3 A single vortex in a two-layer fluid

In another example of the evolution of a solitary vortex at an interface of two fluids of slightly different liquid densities we have for the perturbation $\psi_1^{(1)}$

$$\psi_1^{(1)} \sim \frac{\sqrt{t}}{r} + \frac{e^{it/r^2}}{2i}. \tag{19}$$

Here the last term oscillates and remains small compared to the previous (translational) one for large t. However, it becomes predominant in the expression for the azimuthal velocity $\left(\frac{\partial\psi_1^{(1)}}{\partial r} \sim t\right)$, which results in unlimited growth of oscillations in the vicinity of the vortex. This means that the vortex structure breaks rapidly, which may be treated as a result of the interface "winding" around the vortex nucleus.

2.3.4 A vortex dipole in a density-stratified fluid

Of real practical interest is the problem of the motion of a vortex pair in stratified fluid. Note that if ψ^0 corresponds to a vortex pair, the perturbation $\psi^{(1)}$ remains finite, which is the necessary condition for retaining the structural entity of the vortex dipole. By modifying the asymptotic method for describing the motion of a vortex pair in a weakly inhomogeneous liquid, it is easy to obtain the equations for the center of the vortex pair $\mathbf{r}_0(x_0, y_0, t)$ and the distance $\mathbf{l}(t)$ between vortices (cf. Fig. 7), when the vortex dipole

is moving in the field of the vorticity $h(\mathbf{r},t)$ induced by the dipole in the stratified fluid:

$$\left(\Omega \times \frac{d\mathbf{r}_0}{dt}\right) = \beta_1 \frac{\mathbf{l}}{|\mathbf{l}|^2} \tag{20}$$

and

$$\left(\Omega \times \frac{d\mathbf{l}}{dt}\right) = \beta_2 \int h(\mathbf{r},t) \nabla \Psi_\Sigma^0 d\mathbf{r}, \tag{21}$$

where $\beta_{1,2}$ are constants, Ω is the vorticity in a single vortex, (we assume that $|\Omega| = 1$) and $\Psi_\Sigma^{(0)} = \Psi^{(0)}|\mathbf{r} - \mathbf{r}_{01}| - \Psi^{(0)}|\mathbf{r} - \mathbf{r}_{02}|$ is the stream function of an unperturbed pair. These equations are valid for vortices of an arbitrary form but having a constant vorticity in each of them. The induced vorticity is described by the equation

$$\frac{\partial h}{\partial t} + I(\Psi_{\Sigma,}^{(0)} h) = R$$

(I is the Jacobian).

Further, we consider an important example of the vortex pair interaction with the pycnocline considered as an interface of two fluids of slightly different densities. It is supposed that the pycnocline is positioned far from the vortex pair (compared to its own dimension) and that gravity can be neglected again. An arbitrary direction of the pair axis with respect to the interface is admitted (Fig. 8a). In this case the equation for the vorticity density induced by the perturbation has the form

$$\frac{\partial h}{\partial t} + I(\Psi_\Sigma^{(0)}, h) = \frac{(\nabla p^0 \times \nabla \rho)}{\rho_0^2}, \tag{22}$$

where $\psi_\Sigma = \Gamma \ln[|\mathbf{r} - \mathbf{r}_{01}|/|\mathbf{r} - \mathbf{r}_{02}|]$, $\Gamma = |\Omega|\pi a^2$ is the total vorticity flux (the circulation) for a vortex of radius a, ∇p^0 is the pressure gradient caused by the unperturbed vortex dipole, $\nabla \rho$ is the density perturbation gradient. The density perturbation ρ satisfies the continuity equation

$$\frac{\partial \rho}{\partial t} + I(\Psi_\Sigma^0, \rho) = 0, \tag{23}$$

which should be solved with the initial conditions at the interface $y = 0$:

$$\rho(y) = \rho_1 \qquad y > 0$$

$$\rho(y) = \rho_2 \qquad y < 0$$

so that $\frac{\Delta\rho}{\rho} = \frac{\rho_1 - \rho_2}{\rho_{1,2}} \ll 1$. Further, we shall operate, in the first approximation, with the "frozen" density when the density jump remains fixed during the entire process of the vortex pair propagation. This approximation is valid if the jump is far from the vortex pair. Note that, in fact, the left-hand side of (22) is the total time derivative, and here $\frac{d}{dt}h \sim \nabla\rho\frac{d}{dt}\nabla\Psi^0_\Sigma$, so that in the case of the "frozen" density when the density perturbation depends only on the y coordinate, we have for the induced vorticity:

$$h = \frac{\nabla\rho(y)}{\rho_0}\nabla\psi_\Sigma, \tag{24}$$

where, in this case, $\nabla\rho(y) = \Delta\rho\delta(y)$. The set of equations (20) governing the pair motion appears to have the form

$$\frac{dx_0}{dt} = \Gamma ly/l^2 \tag{25}$$

$$\frac{dy_0}{dt} = -\Gamma lx/l^2$$

$$\frac{dly}{dt} = -\int_-^+\int_{-\infty}^{\infty}\delta(y)\frac{\partial\Psi^0_\Sigma}{\partial x}\times\frac{\partial\Psi^0_\Sigma}{\partial y}dxdy$$

$$\frac{dlx}{dt} = \int_-^+\int_{-\infty}^{\infty}\delta(y)(\frac{\partial\Psi^0_\Sigma}{\partial y})^2dxdy.$$

For the vortex pair located far from the density jump, the spatial distribution of the velocity field is

$$\frac{\partial\Psi^0_\Sigma}{\partial x} = -\Gamma\left[\frac{((y-y_0)^2-(x-x_0)^2)lx - 2(x-x_0)(y-y_0)ly}{(x-x_0)^2+(y-y_0)^2}\right] \tag{26}$$

$$\frac{\partial\Psi^0_\Sigma}{\partial y} = \Gamma\left[\frac{((y-y_0)^2-(x-x_0)^2)ly + 2(x-x_0)(y-y_0)lx}{(x-x_0)^2+(y-y_0)^2}\right].$$

After substituting (26) in (25) we obtain a set of equations describing the motion of the pair in a medium with a jump:

$$\frac{dx_0}{dt} = \Gamma ly/l^2, \tag{27}$$

$$\frac{dy_0}{dt} = -\Gamma lx/l^2, \tag{28}$$

$$\frac{dly}{dt} = 0, \tag{29}$$

$$\frac{dlx}{dt} = \frac{\Gamma}{2}\pi\left[\frac{lx^2 + ly^2}{y_0^2}\right]\frac{\Delta\rho}{\rho}. \tag{30}$$

Let us analyze the system (27-30). It is evident from (29) that the vertical component of the distance l_y between the vortex centers does not vary, i.e., $l_y = l_{y0} = \text{const}$. However, the value of l_x,as well as the total distance l between the nuclei can change. By dividing (30) by (28), we obtain a simple equation describing the variation of the horizontal distance l_x as the pair moves

$$\frac{dlx}{dy_0} = -\frac{\pi}{2}\frac{\Delta\rho}{\rho}\frac{(lx^2 + ly_0^2)}{y_0^3 lx}, \tag{31}$$

(determining the angle of the pair motion on or from the jump):

$$l_x^2 + l_{y0}^2 = \frac{y_0^2}{Cy_0^2 - \frac{\pi}{2}\frac{\Delta\rho}{\rho}}, \tag{32}$$

where $C = \text{const.}$ is determined by the initial conditions, e.g., by the value l^2 or $l_x^2 = l_{x\infty}^2$ for $y_0 \to \infty$

$$C = \frac{1}{l_{x\infty}^2 + l_{y0}^2}. \tag{33}$$

It can easily be seen from (32) that depending on the sign of $\frac{\Delta\rho}{\rho}$, different regimes of the pair motion are possible. If $\frac{\Delta\rho}{\rho} > 0$, l_x^2 may become zero, a regime is possible for which a pair moves from infinity to infinity after reflection from the jump (Fig. 9a). The minimum distance from the pycnocline achieved by the pair before reflection equals

$$(y_0^2)_{\min} = \frac{\pi}{2}\frac{\Delta\rho}{\rho}l_{y0}^2\frac{l^2}{l_{x\infty}^2}.$$

It is evident that because $(y_0^2)_{\min}$ must remain large, our approximation is valid when $\frac{y_0^2 \min}{l^2} \gg 1$. Most interesting here is the case of a grazing incidence

angle when this approximation can work throughout all the stages of the motion.

For another limiting case when $\frac{\Delta\rho}{\rho} > 0$, the relationship $l_x^2(y_0^2)$ is shown in Fig. 9b. Moving from a more dense medium to a less dense one, the pair, according to our solution, achieves the minimum height for which $\dot{l}_x \to \infty$, $\dot{y}_0 \to 0, \dot{x}_0 \to 0$. However, at this stage the distance between the vortices and the interface is small $\left(\frac{y_0^2 \min}{l^2} \ll 1\right)$, which is outside the limits of the applicability of the approximation adopted. But the solution obtained reflects at least the trend to the separation of the nuclei when the pair is approaching the interface.

2.3.5 Conclusions

A theory has been developed for the analytical description of the vortex and vortex pair motion in a weakly stratified fluid, i.e., for situations characteristic of the ocean. The results permit one to estimate the conditions of preserving the entity of the vortex structures or their destruction due to stratification. Dynamics of a vortex pair in the vicinity of a sharp pycnocline is described. In particular, it is shown that if the vortex pair located far from the interface is incident from the less dense medium toward a more dense one at small (grazing) angles, it "feels" a jump even at relatively large distances in such a way that it becomes reflected and goes back as a whole, but with a varying distance between the vortex nuclei. The models considered seem to be important for understanding the motion of vortex structures shed off the obliquely oriented parts of submerged apparatuses, and of the thermics in ocean and atmosphere. Future research will consider the vortices in a smoothly stratified fluid and take into account gravity effects, including the excitation of internal waves by vortex structures in the upper ocean.

3 Experimental studies

3.1 Experimental investigation of intense, short surface wave trains

The propagation of intense, deep-water gravity wave trains was investigated in numerous experiments (see, for example, [27, 28]). These experimental results are usually interpreted by the known nonlinear Schrödinger equation (NSE) obtained in the framework of the second (parabolic) approximation of the nonlinear dispersion theory [28, 29]:

$$2i\frac{\partial a}{\partial t}+\frac{\omega_0}{4k_0^2}\frac{\partial^2 a}{\partial \xi^2}+\omega_0 k_0^2\left|a\right|^2 a=0,$$

where a is the complex wave amplitude, $\xi = x - V_g^L t$, $\omega_0^2 = gk_0$, V_g^L is the linear group velocity of a gravity wave at frequency ω_0. However, there exists a discrepancy between experimental results and the theoretical model. The discrepancy is associated with the wave-train asymmetry arising even for initially symmetrical wave train. This effect cannot be explained in terms of the classical NSE. For this equation, under a symmetrical initial condition

$$a\left(\xi,\ 0\right)=a\left(-\xi,\ 0\right),$$

only symmetrical deformation of the envelope $a\left(\xi,\ t\right)$, i.e.,

$$a\left(\xi,\ t\right)=a\left(-\xi,\ t\right),$$

is possible.

The above-mentioned asymmetry in the wave-train shape can be explained by considering the third-order approximation. The envelope equation for an intense, deep-water gravity wave in the third-order approximation of the nonlinear dispersion theory has the following form ([30]):

$$2i\left(\frac{\partial a}{\partial t}+\frac{5}{2}V_g^L k_0^2\left|a\right|^2\frac{\partial a}{\partial \xi}\right)+\frac{\omega_0}{4k_0^2}\frac{\partial^2 a}{\partial \xi^2}+\omega_0 k_0^2\left|a\right|^2 a-i\frac{\omega_0}{8k_0^3}\frac{\partial^3 a}{\partial \xi^3}+$$

$$+\omega_0 k_0 a\lim_{s\to 0}\int_{-\infty}^{\infty}\left|a\left(\xi^{'},t\right)\right|^2\frac{\left[\left(\xi-\xi^{'}\right)^2-s^2\right]}{\left[\left(\xi-\xi^{'}\right)^2+s^2\right]^2}d\xi^{'}=0. \qquad (34)$$

This equation has an asymmetrical solution even for a symmetrical initial wave train. For a detailed comparison with this theory, more detailed information about the shape of the wave train is needed.

Our experiment was carried out in the large IAP tank that measured $20 \times 4 \times 2$ m^3.(see Fig. 10 and the first memorandum [1]). The gravity wave trains were generated by a wave maker at one tank end and absorbed at the other end. The trains were generated by five oscillations of the wavemaker at the frequency $\nu = 1.6$ Hz ($\lambda = 58.5$ cm, $V_g^L = 48$ cm/s). The phase velocity of deep-water gravity waves V_p^L is twice as large as the group velocity V_g^L: therefore, the initial spatial length of the wave train was only $2.5\lambda = 145$ cm. The water surface displacements were measured at distances of 4 m, 6 m, 8 m, 10 m from the wave maker. Figures 11(a,b,c) present the oscillograms of water surface displacement at different distances. Records (1) correspond to the distance $L = 4$ m, (2) $- L = 6$ m, (3) $- L = 8$ m, (4) $- L = 10$ m. Three levels of the initial amplitude were used: 3 cm, 2 cm, and 1 cm. In the train of maximum amplitude (3 cm) (Fig. 11a), the leading front of the envelope at the distance 6 m significantly steepens [Fig. 11a, (2), (3)]; at larger distances, an intense short pulse was formed at the leading edge [Fig. 11b, (4)]. For the initial amplitude of 2 cm, the distortion of the pulse envelope was weaker (Fig. 11c). For the amplitude of 1 cm, the shape of the wave train envelope remained almost undistorted. The dependence of the energy center coordinate

$$\overline{x\,(t)} = \frac{1}{N_0} \int\limits_{-\infty}^{+\infty} x\,|\psi|^2\,dx,$$

(here $N_0 = \int\limits_{-\infty}^{+\infty} |\psi|^2\,dx$) on real time in the course of propagation is shown in Fig. 12 for two different values of the water surface displacement, $a = 1$ cm and 3 cm (curves 1 and 2, respectively). The velocity of the wave train center increased with its amplitude. Namely, the velocity of the wave train for the initial amplitude of 3 cm was by

$$\overline{\Delta V}^{NL} \simeq 5 \text{ cm/s},$$

larger than that for the initial amplitude of 1 cm, which corresponds to an

11% increase from the linear group velocity of gravity waves V_g^L for this frequency.

To compare the dependence of the wave-train shape distortions and the velocity of gravity waves on their intensity with the third-order theory prescriptions, we plan to perform numerical simulation on the basis of Dysthe's equation. This will permit us to create more realistic models of surface wave intermittency on the sea surface.

3.2 Experimental investigation of amplitude dispersion of gravity surface waves

The "amplitude dispersion" of surface waves (i.e., the dependence of the wave phase velocity on its amplitude) is an important characteristic affecting the wind-wave spectra. The experiments (see [31, 32]) have demonstrated a discrepancy between the measured values of the wave velocity and calculations based on the linear theory. One of the main causes of this discrepancy is hydrodynamic nonlinearity. As has been shown in laboratory experiments [33], the observed anomalies of phase velocities of wind waves can be a result of nonlinear wave interaction. Despite detailed consideration of surface wave interactions in literature (see, e.g., [34], where the "parametric" interpretation of the interaction was discussed as a convenient way to estimate the energy exchange between waves), the effects of interactions on the dispersion characteristics of surface waves has not yet been considered. In this connection it seems important to evaluate the agreement between the experiment and the nonlinear theory of wave interaction in what concerns the amplitude dispersion effects. This was the main goal of our experiments.

Below, the measurement results are presented for the nonlinear additions to the phase velocity in the simplest case of the interaction of wave pairs with equal frequencies ω and amplitudes A, but with different wave numbers $\vec{k}$. It has been found that in this case the quantitative agreement with the nonlinear theory [29] takes place only for a traveling wave (the self-action effect for $k_1 = k_2$); in a standing wave not only quantitative but also qualitative discrepancies between the theory and experiment have been revealed. A possible cause of these discrepancies has been discussed.

3.2.1 Experiments with a travelling wave

A wave close to sinusoidal with the fundamental frequency f= 2.5 Hz (wavelength λ =0.25 m) was generated by a mechanical wave maker at one end of a tank (channel) with length L =3 m, width 0.2 m and depth H =0.4 m. At the other end the wave was effectively absorbed by a wave damper: the reflected wave amplitude did not exceed ~3% of the incident one. Nonlinear additions to the linear phase velocity $v(0)$ were measured by two-string wave gauges spaced at a distance $L_0 = 5v\,(0)\,f^{-1} = 5\lambda$ apart (Fig. 13a). At small amplitudes the liquid surface oscillations at both strings occurred in phase. For larger A there was a measurable phase difference between oscillations, the value of which was used to determine the relative nonlinear addition to the phase velocity

$$\frac{\triangle v(A)}{v(0)} = \frac{1}{5}\triangle t \cdot f,$$

where $\triangle t$ is the time interval between the nearest maxima of signal oscillations of the first and second sensors. The quantitative measurements were carried out using the Bruel & Kjer 2034" spectrum analyzer the amplitude scale of which was calibrated by elevating a string by (1.8±0.2) cm in the absence of the wave. The oscillation frequency of the wave maker was assigned by the GZ-102 external generator with an absolute accuracy of 10^{-3} Hz. The results of measuring the ratio $\frac{\triangle v(A)}{v(0)}$ are given in Fig. 14.

3.2.2 Experiments with a standing wave

The dependence of resonance frequency f_0 on amplitude A at a fixed wave number k was measured in a resonator of length L_0 formed by two reflecting walls inside the channel described above. Weak coupling between the resonator and the wave makers was provided by a transverse plate placed at a distance L_o from the tank wall and submerged in water at a depth $\triangle H$= 7 cm (Fig. 13b). At the depths $\mid z \mid \sim \triangle H$ the wave maker generated a pulsating horizontal motion of the liquid, which, in turn, produced a standing wave. In the resonator, the amplitude of free oscillations at the second mode ($\lambda = L_0$) decreased by e times during approximately 50 periods. The energy loss is mainly caused by incomplete wave reflection from the partly submerged wall and the presence of a film of a surface-active substance. The experiments were carried out with two resonators with lengths L_0 = 17.1 cm

and $L_0 = 30$ cm. The dependence of the oscillation amplitude of the standing wave on the frequency was measured at a fixed amplitude of the external generator. A set of corresponding resonance curves for the case L_0 =17.1 cm is shown in Fig. 15. The maxima of the curves correspond to standing waves of various resonance frequencies f_0 and amplitudes A, but of equal wave numbers $k = \pi/L_0$. After the measurement results were processed, the dependence $f_o(A)$ was constructed. The value $f_o(0)$ was determined by the continuation of this curve to the intersection with the abscissa and then the relative nonlinear addition to the frequency was calculated

$$\frac{f_0(A) - f_0(0)}{f_0(0)} = \frac{v(A) - v(0)}{v(0)},$$

which is equal to the relative nonlinear addition to the phase velocity $v\,(0)$ of each component of the standing wave (which, of course, depends on the amplitudes of both waves for each of them). The dependence of this ratio on wave amplitude for the standing wave is plotted in Fig. 14.

3.2.3 Calculation of phase velocity and comparison of theory with experiment

The nonlinear effects in surface waves are due to the nonlinear boundary condition on the free surface of the liquid. As is known [36, 37], the exact boundary condition for an ideal liquid is defined by the Bernoulli equation; approximate boundary conditions are obtained by the expansion of this equation in the Taylor series in the vicinity of the horizontal plane $z = 0$, coinciding with the unperturbed liquid surface. The small parameter here is the wave steepness kA.

Surface waves can be considered as linear only if the steepness is small. In this case by using the Laplace equation $\nabla^2\varphi = 0$, the linearized boundary condition on the plane z =0

$$\frac{\partial^2\varphi}{\partial t^2} + g\frac{\partial\varphi}{\partial z} = 0 \tag{35}$$

and the condition at the bottom $\frac{\partial\varphi}{\partial z}\,|_{z=H}$ for waves in deep water, one can obtain the known dispersion relation

$$\omega = \sqrt{g_o k},$$

where g_o is the acceleration of gravity. The frequency $\omega = 2\pi f$ depends on the wave amplitude A if the boundary condition is written with an accuracy to φ^3 inclusive (the appropriate expression is available, for example, in [37] and is not given here because of its complexity). In this case we have

$$\omega(k, A) = \sqrt{g_o k}, \left[1 \pm 0.5 (kA)^2\right], \tag{36}$$

where the + sign refers to the traveling wave, while the - sign refers to the standing wave.

Now we move on to the measurement results. In the case of the traveling wave, there is good agreement between the calculation by formula (36), the dashed line in Fig. 14, and the experiment. In the case of the standing wave there is both a quantitative and a qualitative difference between the corresponding data: at small kA the measured relative addition to the frequency exceeds approximately three times the calculated values (the dashed line in 14), while at rather large kA the dependence of $\Delta f/f$ on $(kA)^2$ is essentially different from the linear one.

In order to explain the cause of the above discrepancies, we have carried out an albeit rough but physically clear estimate of the amplitude dispersion by employing the known nonlinear effects in waves: the generation of the mean horizontal flow, and vertical oscillations of a liquid with double frequency. Let us consider the interaction of two plane waves

$$\eta_{1,2} = A \cos(ky \sin\theta \pm kx \cos\theta - \omega t)$$

being different only in regard to the propagation direction characterized by the angle θ to the x axis. The position of the y axis is chosen here to be symmetric with respect to the directions of wave propagation, as is shown in Fig. 16. In this case, the total displacement has a form

$$\eta = \eta_1 + \eta_2 = 2A \cos(kx \cos\theta) \cos(ky \sin\theta - \omega t)$$

and the potential

$$\varphi^{(1)} = 2A\omega k^{-1} \cos(kx \cos\theta) \sin(ky \sin\theta - \omega t)\, e^{kz} \tag{37}$$

(z-axis is directed upwards).

The motion of an individual particle in the wave η is described by the equations for Lagrangian coordinates x_o, y_o, z_o:

$$\dot{x} = u(x_o, y_o, z_o),$$

$$\dot{y} = v\left(x_o, y_o, z_o\right), \tag{38}$$
$$\dot{z} = w\left(x_o, y_o, z_o\right).$$

Deviations of particles (x_o,y_o,z_o) from the initial position (x,y,z) do not exceed the wave amplitude; thus the equations (38) can be expanded in the Taylor series in the vicinity of $(x.y,z)$ while retaining only the terms of the order of $(kA)^2$. Assuming further that the first-order velocity values $u^{(1)} = \frac{\partial\varphi^{(1)}}{\partial x}, v^{(1)} = \frac{\partial\varphi^{(1)}}{\partial y}, w^{(1)} = \frac{\partial\varphi^{(1)}}{\partial z}$ in the vicinity of the point $(x.y.z)$ do not depend on (x_o,y_o,z_o), we obtain

$$\dot{x} = u^{(1)}$$
$$\overline{\dot{y}} = v^{(1)} + A^2\omega k e^{2kz}\sin\theta$$
$$\dot{z} = w^{(1)} + 2A^2\omega k e^{2kz}\cos^2\theta\sin 2\left(ky\sin\theta - \omega t\right),$$

where the overline denotes averaging of the y-component over the horizontal coordinates. As is seen, in addition to periodic motions with velocities $u^{(1)},v^{(1)},w^{(1)}$ and the frequency ω, the liquid particles move, on average, in the horizontal plane (the Stokes flow) with the velocity

$$v^{(2)} = 2v\left(0\right)\left(kA\right)^2 e^{2kz}\sin\theta$$

and oscillate vertically with the double frequency 2ω

$$w^{(2)} = 2v\left(0\right)\left(kA\right)^2 e^{2kz}\cos^2\theta\sin 2\left(ky\sin\theta - \omega t\right),$$

where $v\left(0\right) = \omega k^{-1}$ is the phase velocity of the wave. These particle motions correspond to two mechanisms of the amplitude dispersion, one of which in its "pure" form is revealed in a traveling wave, while the other is in a standing wave. In the case of a traveling wave, the components $\eta_{(1)}$ and η_2 propagate in the same direction, thus $\theta = 90^o$ and $w^{(2)} = 0$, while $v^{(2)} = v\left(0\right)\left(\sqrt{2}kA\right)^2 e^{2kz}$. As is mentioned in [35], the phase velocity of a traveling wave may increase due to the Stokes flow. This explanation of the self-action effect can now be easily confirmed by the calculation. Let a traveling wave still remain close to harmonic, but a shear flow $v^{(2)}$ be present. The variation of the phase velocity of the wave caused by this flow is [33]

$$\triangle v\left(A\right) = v_o^{(2)} - \int_{-\infty}^{0}\frac{\partial v^{(2)}}{\partial z}e^{2kz}dz = \frac{1}{2}v\left(0\right)\left(kA\right)^2, \tag{39}$$

where $v_o^{(2)}$- the Stokes flow at $z = 0$, which coincides with (36). Note that in the case of a constant flow U_o independent of the flow depth, the addition to the traveling wave velocity equals

$$\triangle v = U_o.$$

If the shear flow is nonstationary, the time differentiation of (39) yields the depth-average of horizontal acceleration component g_x of liquid particles:

$$g_x = g_x\,(z = 0) - \int_{-\infty}^{0} \frac{\partial g_x}{\partial z} e^{2kz} dz. \tag{40}$$

Let us now consider the case of the counterpropagating motion of the waves η_1 and η_2; it corresponds to the angle $\theta = 0$. The Stokes flows generated by the waves η_1 and η_2 are directed oppositely here; thus $v^{(2)}= 0$. Vertical oscillations of particles at the frequency 2ω have a maximum amplitude. They generate a dynamic acceleration field at the depths $\mid z \mid \geq 0$

$$G_1 = -4\,(kA)^2\, g_o e^{2kz} \cos 2\omega t, \tag{41}$$

which, as will be shown below, leads to amplitude dispersion of the standing wave, according to the formula (36). The frequency variations in addition to (36) are due to the liquid motion in the "amplitude" layer $z = \pm 2A$, the result of which is the pressure component $p^{(2)} \sim (kA)^2$ varying with the frequency 2ω and independent of depth [36]. This pressure is formally determined by the potential

$$\varphi = \varphi^{(1)} + \varphi^{(2)} = \varphi^{(1)} + A^2\omega \cos^2\theta \sin 2\,(ky \sin\theta - \omega t)\,, \tag{42}$$

which satisfies the nonlinear boundary condition written with an accuracy to φ^2 inclusive (see [37])

$$\frac{\partial^2\varphi}{\partial t^2} + g_o \frac{\partial\varphi}{\partial z} + 2\nabla\varphi\nabla\frac{\partial\varphi}{\partial t} - \frac{1}{g_o}\frac{\partial\varphi}{\partial t}\left(\frac{\partial^3\varphi}{\partial t^2\partial z} + g_o\frac{\partial^2\varphi}{\partial z^2}\right) = 0.$$

It follows from (42) that

$$p^{(2)} = \rho_o \frac{\partial\varphi}{\partial t} = -2\rho_o A^2\omega^2 \cos^2\theta \cos 2\,(ky \sin\theta - \omega t)\,. \tag{43}$$

The same expression can be obtained by integrating the equation for the vertical component of the liquid momentum, which yields the formula [36]:

$$p^{(2)} = \rho_o \frac{\partial}{\partial t} \overline{\eta \omega_o},$$

where the overline means averaging over horizontal coordinates, and ω_o is the vertical velocity of the liquid at the level $z = 0$.

In fact, the pressure $p^{(2)}$ is developed in the "amplitude" layer $\triangle z = 4A$, being zero at $z = 2A$ and achieving a maximum amplitude at $z = -2A$. We shall take into account these dynamics phenomenologically by multiplying (43) by the function

$$\Phi(z) = 1 - e^{\frac{z-0.5DA}{DA}},$$

where D is an empirical coefficient characterizing the effective layer thickness. Then, according to the Euler equation, the pressure $p^{(2)}$ corresponds to the acceleration field

$$G_2 = -\frac{1}{\rho_o} \frac{dp^{(2)}}{dz} = -\frac{2}{D} A\omega^2 e^{\frac{z-0.5DA}{DA}} \cos 2\omega t. \tag{44}$$

The total homogeneous field of vertical acceleration in a standing wave can be found from the above formulas (41) and (44) after integrating over z according to (40). (We suppose that it is valid for the vertical acceleration component as well):

$$\overline{G} = \overline{G}_1 + \overline{G}_2 = g_0 \left[1 - 2(kA)^2 \cos 2\omega t - \frac{4(kA)^2}{1 + 2DkA} \cos 2\omega t \right].$$

Here the overline means averaging of the accelerations G_1 and G_2 over the vertical coordinate.

This vertical acceleration field modulates the wave potential with a double frequency, and the parametric resonance takes place for the standing wave. For a Fourier component of the potential, $\hat{\varphi}_n = \varphi e^{-ikx}$, the Mattieu equation is valid:

$$\frac{1}{g_o k} \frac{\partial^2 \hat{\varphi}}{\partial t^2} + (1 - q \cos 2\omega t) \hat{\varphi} = 0,$$

which follows from the linear boundary condition (35) taking into account the expression for $\overline{G}$, so that $q = 2(kA)^2 + \frac{4(kA)^2}{1+2DkA}$. We substitute the solution in the form [10]

$$\hat{\varphi} = Ae^{-i\omega t} + \sum_{n=1}^{2} \left[q^n B^{(n)} e^{-i(n\Omega-\omega)t} + q^n C^{(n)} e^{-i(n\Omega+\omega)t} + \text{c.c.} \right],$$

where $\Omega = 2\omega$, and take into account only the fundamental and parametric (subharmonic) resonance at the frequency ω. As a result of calculations we obtain:

$$\omega = \sqrt{g_o k} \left[1 - \frac{1}{2}(kA)^2 - \frac{(kA)^2}{1+2DkA} \right]. \tag{45}$$

The nonlinear dispersion relation (45) differs from (36) by the additional term responsible for vertical oscillations of the liquid surface. This relation satisfactorily agrees with experimental data both for small and relatively large (kA) when $D < 4$ (Fig. 14).

To specify the coefficient D, one should measure the pressure amplitude $p^{(2)}$ together with the nonlinear addition to the frequency, since the value of $p^{(2)}$ can be affected by a film of a surface-active substance always present in the experiment. The development of a stricter theory of this effect is planned for future studies.

3.3 Conclusions

The experimental part of the work at this stage concentrated on the investigation of nonlinear, deep-water surface waves. At least two nontrivial, in our opinion, experimental results have been obtained. The first is self-steepening of a short surface-wave train in the course of propagation, which can be described by a third-order dispersion theory rather than by a classical, nonlinear Shrödinger equation, which is commonly used in similar cases. The second is the much stronger dependence on its intensity of the wave phase velocities in a standing surface wave than that in a traveling wave. A rough theoretical model is suggested to explain this effect based on taking into account the depth-independent pressure at the double frequency formed in the thin "amplitude" layer then interacting parametrically with the main wave. These peculiarities seem to be important for the description of gravity

wave spectra on the ocean surface. In particular, a possible discrepancy with commonly used theoretical formulas for standing waves would indicate the similar (albeit smaller) discrepancy for the waves interacting under an arbitrary angle (except for the collinear propagation), which may directly affect the spectra of the wind waves in the inertial interval, including the weak wave turbulence. Note that our preliminary experiments with two wave pairs have already demonstrated that at the small steepness of the interacting waves, the growth rate of the amplitude of a weak wave pair due to interaction with a strong pair may exceed by several times the prediction of the nonlinear theory. Thus, the necessity is evident to specify the influence of the observed processes on the energy exchange of waves.

4 Acknowledgments

The cooperation with NOAA Environmental Technolology Laboratory and the support from the joint NOAA/DOD Advanced Sensor Application Program are greatly appreciated.

References

[1] Laboratory modeling and theoretical studies of wave interactions in the ocean. Part 1. Experimental Design and Program (L. A. Ostrovsky, Editor). *NOAA Technical Memorandum* ERL ETL-278, Environmental Technology Laboratory, Boulder, CO, 1997,

[2] Stepanyants, Yu. A., Sturova I. V., and Teodorovich E. V., Linear theory of surface and internal wave generation. *Itogi Nauki i Tekhniki, ser. Mekh. Zhidk. i Gaza*, 1987, v. 21, 93-179.

[3] Gorodtsov, V. A., and Teodorovich, E. V., To the wave drag theory (surface and internal waves). In *N. E. Kochin and Development of Mechanics*, Moscow, Nauka, 1984, 131-149.

[4] Reznik, S. N., and Troitskaya, Yu. I., The wave impedance of a localized bottom heterogeneity in a stratified shear flow with a critical layer. *Izv. RAN, Fizika Atm. i Okeana*, 1996, v. 32, 133-140.

[5] Miles, J. W., On the stability of heterogeneous shear flow. *J. Fluid Mech.*, 1961, v. 10, Pt. 4, 496-509.

[6] Howard, L. N., Note to a paper of John Miles. *J. Fluid Mech.*, 1961, v. 10, Pt. 4, 509-514.

[7] Landau, L. D., and Lifshits, I. M., *Hydrodynamics*, Moscow, Nauka, 1986.

[8] Hazel, P., The effect of viscosity and heat conductivity on internal gravity waves at a critical layer. *J. Fluid Mech.*, 1967, v. 30, 775-783.

[9] Maslowe, S. A., Critical layers in shear flows. *Ann. Rev. Fluid Mech.*, 1986, v. 18, 405-432.

[10] Booker, J. R., and Bretherton, F. P., The critical layer for internal gravity waves in a shear flow. *J. Fluid Mech.*, 1967, v. 27, 513-539.

[11] Lin, C. C. *The theory of hydrodynamic stability*, Cambridge Univ. Press, Cambridge, England, 1955.

[12] Reznik, S. N., and Troitskaya Yu. I., Wave drag of a plane localized source moving in a stratified shear flow with a critical layer. *Preprint no. 373*, Inst. Appl. Phys. Russian CAD. Russian Acad. Sci., Nizhny Novgorod, 1995.

[13] Auton, T. R., Hunt, J. C. R., and M.Prud'homme, The force exerted on a body in inviscid unsteady non-uniform rotational flow. *J. Fluid Mech.*, 1988, v. 197, 241-257.

[14] Turner, J. S., Buoyancy effects in fluids. Cambridge University Press, Cambridge, England, 1973.

[15] Ivanov, A. V., Lebedev, A. B., and Ostrovsky, L. A., Experimental study of laminar vortex couple motion in stratified fluid. *Izvestia AN SSSR: Mechanica Zhidkosti i Gaza*, 1985, no. 2, p. 183.

[16] Baranov, S. A., Ivanov, A. V., and Kazakov, V. I., The generation of internal waves by vortices: laboratory modelling and numerical simulation. In: Methods of Hydrophysical Research, Turbulence and Mi-

crostructure (A. V. Gaponov-Grekhov, and S. A. Khristianovich, Editors). Institute of Appl. Phys., Russian Acad. Sci., N. Novgorod, 1990, 117-128.

[17] Baranov, S. A., Kazakov, V. I., and Stepanyants, Yu. A. Internal wave generation by a thermal source in a laboratory tank. In: Methods of Hydrophysical Research, Turbulence and Microstructure (A. V. Gaponov-Grekhov and S. A. Khristianovich, Editors). Institute of Appl. Phys., Russian Acad. Sci., N. Novgorod, 1990, 203-215.

[18] Lamb, H., *Hydrodynamics.* Cambridge University Press, Cambridge, England, 1995.

[19] Batchelor, G. K., *Fluid Dynamics.* Cambridge University Press, Cambridge, England, 1967.

[20] Melander, M. V., Stycrek, A. S., and Zabusky, N. J., Elliptical desingularized vortex model for two-dimensional Euler equation. *Phys. Rev. Lett.*, 1984, v. 53, no. 13, p. 1222.

[21] Saffman, P. G. The motion at a vortex pair in stratified atmosphere. *Studies in Appl. Math.*, 1972, no. 2, 107-119.

[22] Hill, F. M., A numerical study of the descent of a vortex pair in a stratified atmosphere. *J. Fluid Mech.*, 1975, v. 71, no. 1, 1-13.

[23] Dahm, W., Scheil, J. A., and Tryggyason, Dynamics of vortex interaction with a density interface. *J. Fluid Mech.*, 1989, v. 205, 1-43.

[24] Kurgansky, M. V., On vortex pair motion under the surface of heavy fluid. *Izv. AN SSSR: Mech. Zhidk. i Gaza*, 1986, no. 5, 184-187.

[25] Gorshkov, K. A., and Ostrovsky L. A., Interaction of solitons in nonintergrable systems, *Physica D*, 1981, v.3, no. 1, p. 428.

[26] Gorshkov, K. A., and Ostrovsky, L. A., Theory of perturbation for solitons and vortices. in *Metods of Hydrophysical Research. Turbulence and Microstructure* (A. V. Gaponov-Grekhov, S. A. Khristianovitch, and L. A. Ostrovsky, Editors). IAP, N. Novgorod, 1990, 141-160.

[27] Feir, J. E., Discussion: Some results from a wave pulse experiment. *Proc. R. Soc. London*, 1967, v. A299, 54-60.

[28] Benjamin, T. B., and Feir, J. E., The disintegration of wave trains on deep water. Part 1. Theory. *J. Fluid Mech.*, 1967, v. 27, 417-430.

[29] Yuen, H. C., and Lake, B. M. Nonlinear dynamics of deep-water gravity waves. *Advances in Applied Mechanics*, 1982, v. 22, 67-229.

[30] Dysthe, K. B., Note on a modification to the nonlinear Schrödinger equation for application to deep water waves. *Proc. R. Soc. Lond.*, 1979, v. A369, 105-114.

[31] Grose, P. L., Warsh, K. L., and Garstand, M., Dispersion relations and wave shape. *J. Geophys. Res.*, 1972, v. 77, 3902-3906.

[32] Efimov, V. V., Soloviev, Yu. P., and Khristoforov, G. N., Experimental determination of phase velocity of propagation of spectral components of sea waves. *Izv. AN SSSR, Fizika Atmosfery i Okeana*, 1972, v. 8, no. 4, 435-446.

[33] Grawford, D. R., Lake, B. M., Saffman, P. G., and Yuen, H. C., Effects of nonlinearity and spectral bandwidth on the dispersion relation and component phase speeds of surface gravity waves. *J. Fluid Mech.*, 1981, v. 112, 1-32.

[34] Hasselmann, D. E., The high wavenumber instabilities of a Stokes wave. *J. Fluid Mech.*, 1979, v. 93, 491-499.

[35] Longuet-Higgins, M. S., and Phillips, O. M., Phase velocity effects in tertiary wave interactions. *J. Fluid Mech.*, 1962, v. 12, 333-336.

[36] Phillips, O. M., The Dynamics of the Upper Ocean. Cambridge University Press, Cambridge, England, 1977.

[37] Newman, J. N., Marine Hydrodynamics. MIT Press, Cambridge, Massachusetts, 1977.

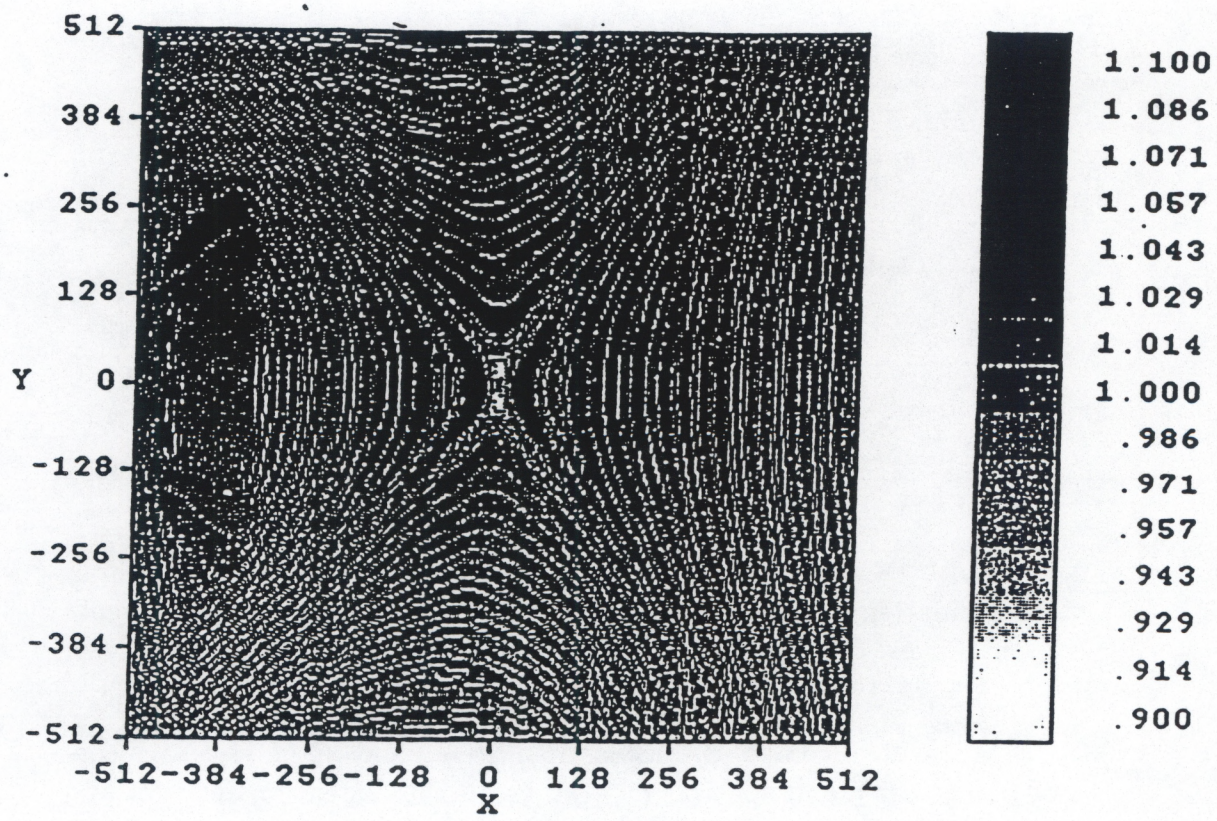

Fig. 1a. Spatial distribution of modulus of surface wave-field amplitude $|a|\left(\tilde{x},\tilde{y}\right)$ for $\tilde{k}_{x0}= 1$, $\tilde{k}_{y0}= 0$, $c = 2$, $\tilde{h} = 10$ $\tilde{t}= 900$.

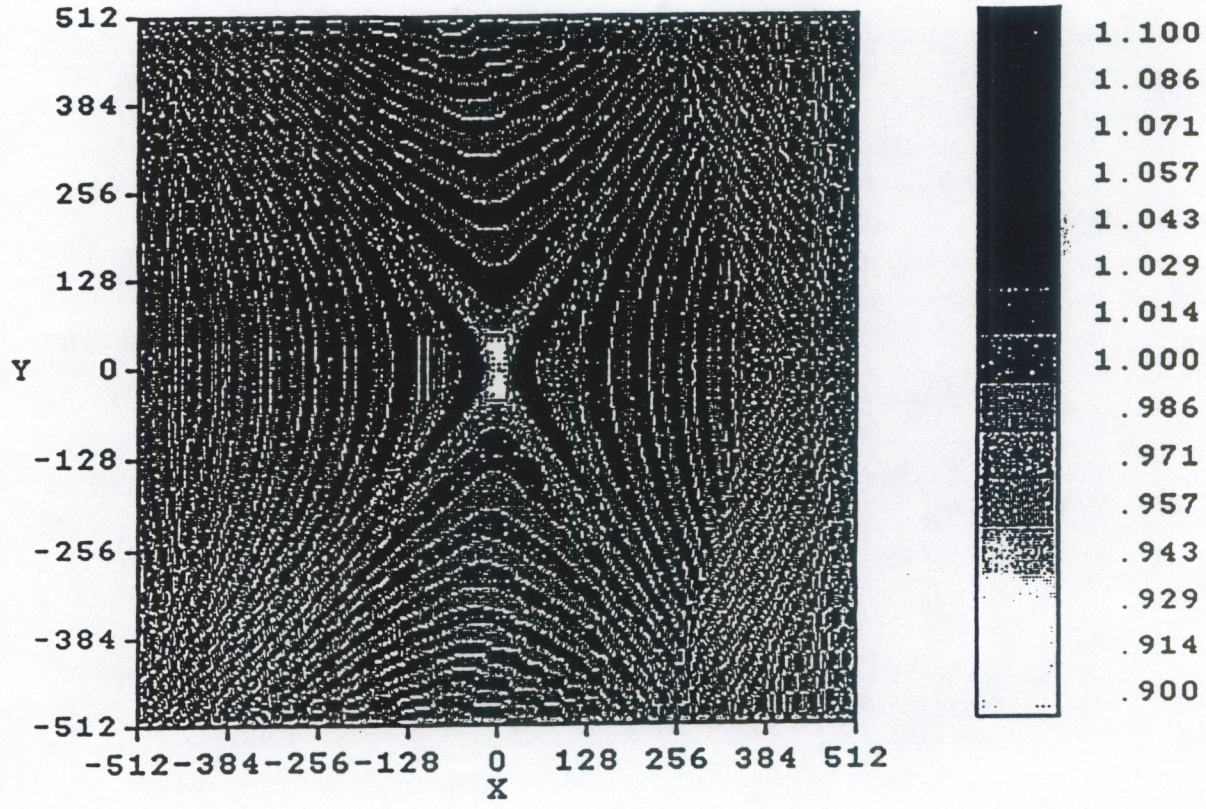

Fig. 1b. Spatial distribution of modulus of surface wave-field amplitude $|a|\left(\tilde{x},\tilde{y}\right)$ for $\tilde{k}_{x0}= 1$, $\tilde{k}_{y0}= 0$, $c = 2$, $\tilde{h} = 10$ $\tilde{t}= 1500$.

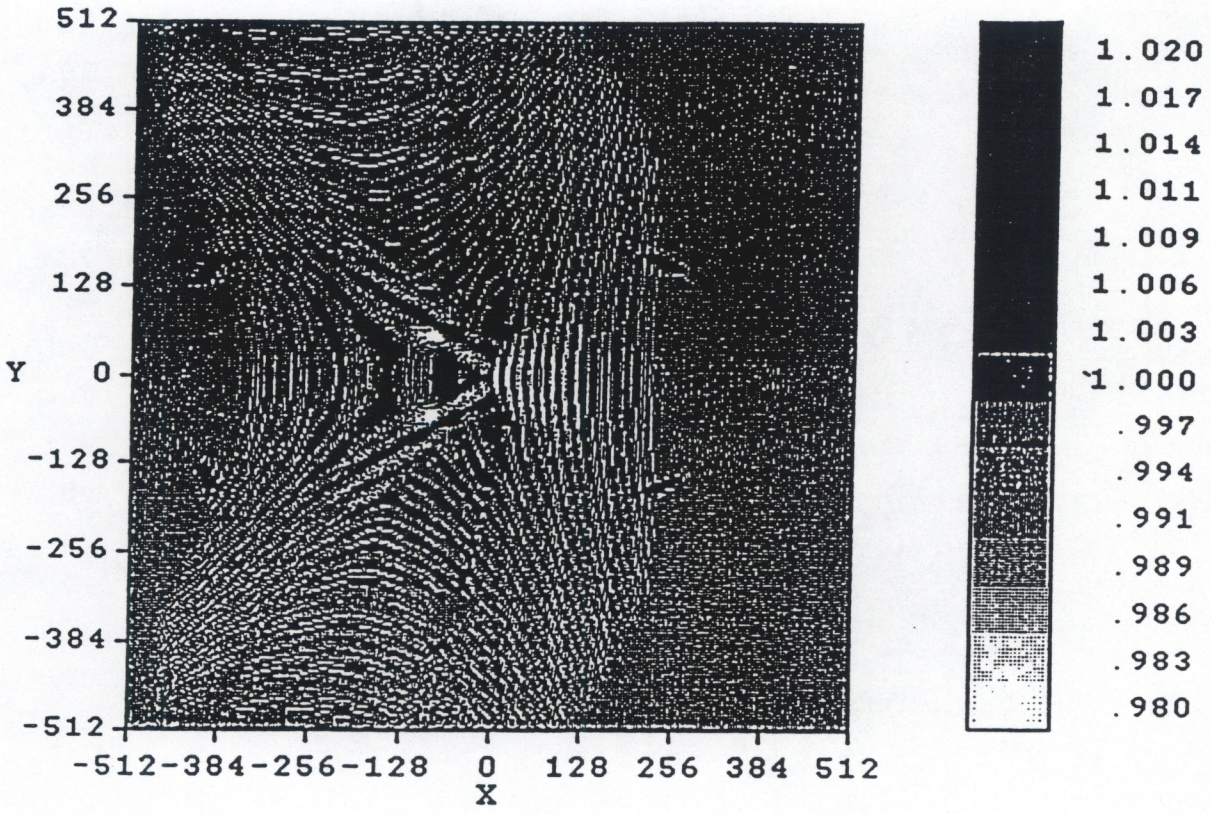

Fig. 1c. Spatial distribution of modulus of surface wave-field amplitude $|a|\left(\tilde{x},\tilde{y}\right)$ for $\tilde{k}_{x0}$= 1.2, $\tilde{k}_{y0}$= 0, c = 2, $\tilde{h}$ = 10 $\tilde{t}$= 1500.

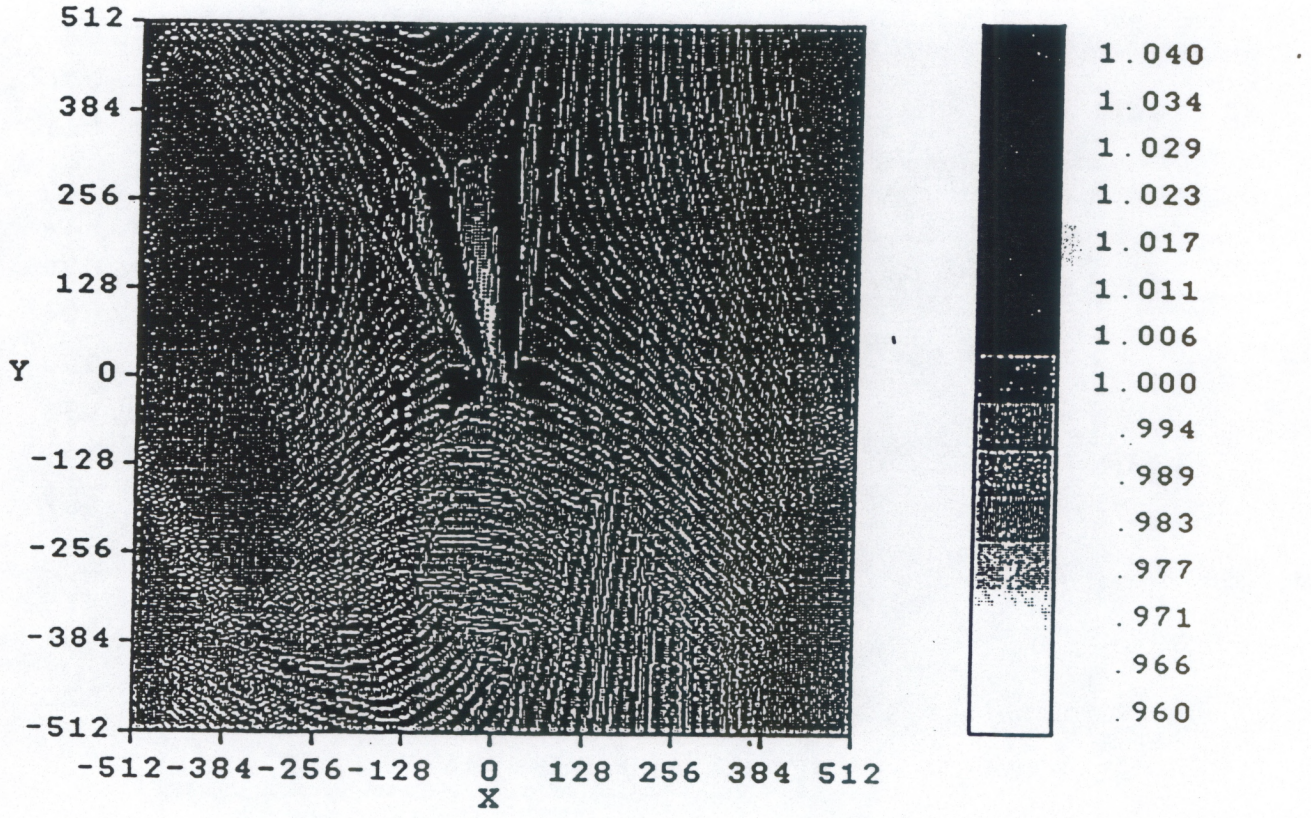

Fig. 1d. Spatial distribution of modulus of surface wavefield amplitude $|a|\left(\tilde{x},\tilde{y}\right)$ for $\tilde{k}_{x0}$= 1, $\tilde{k}_{y0}$= 0.2, c = 2, $\tilde{h}$ = 10 $\tilde{t}$= 1500.

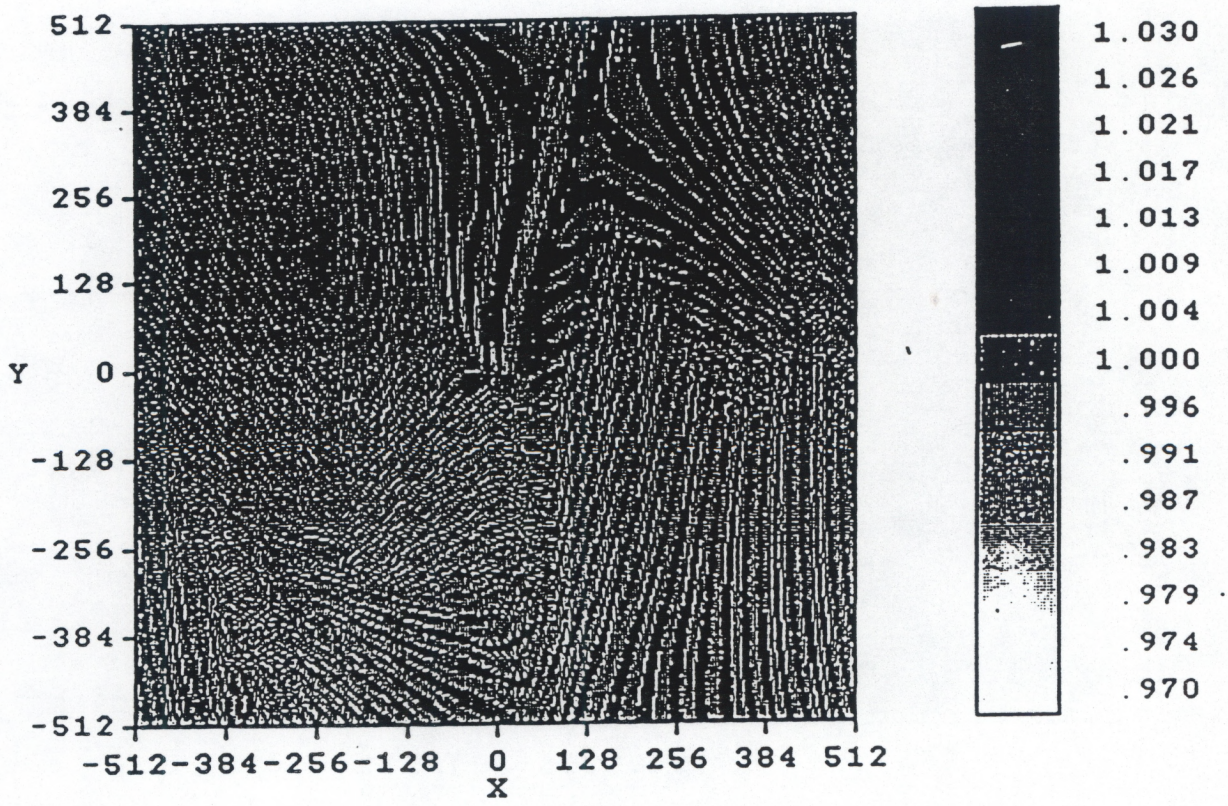

Fig. 1e. Spatial distribution of modulus of surface wave-field amplitude $|a|\left(\tilde{x},\tilde{y}\right)$ for e) $\tilde{k}_{x0}$= 0.8, $\tilde{k}_{y0}$= 0.2, c = 2, $\tilde{h}$ = 10

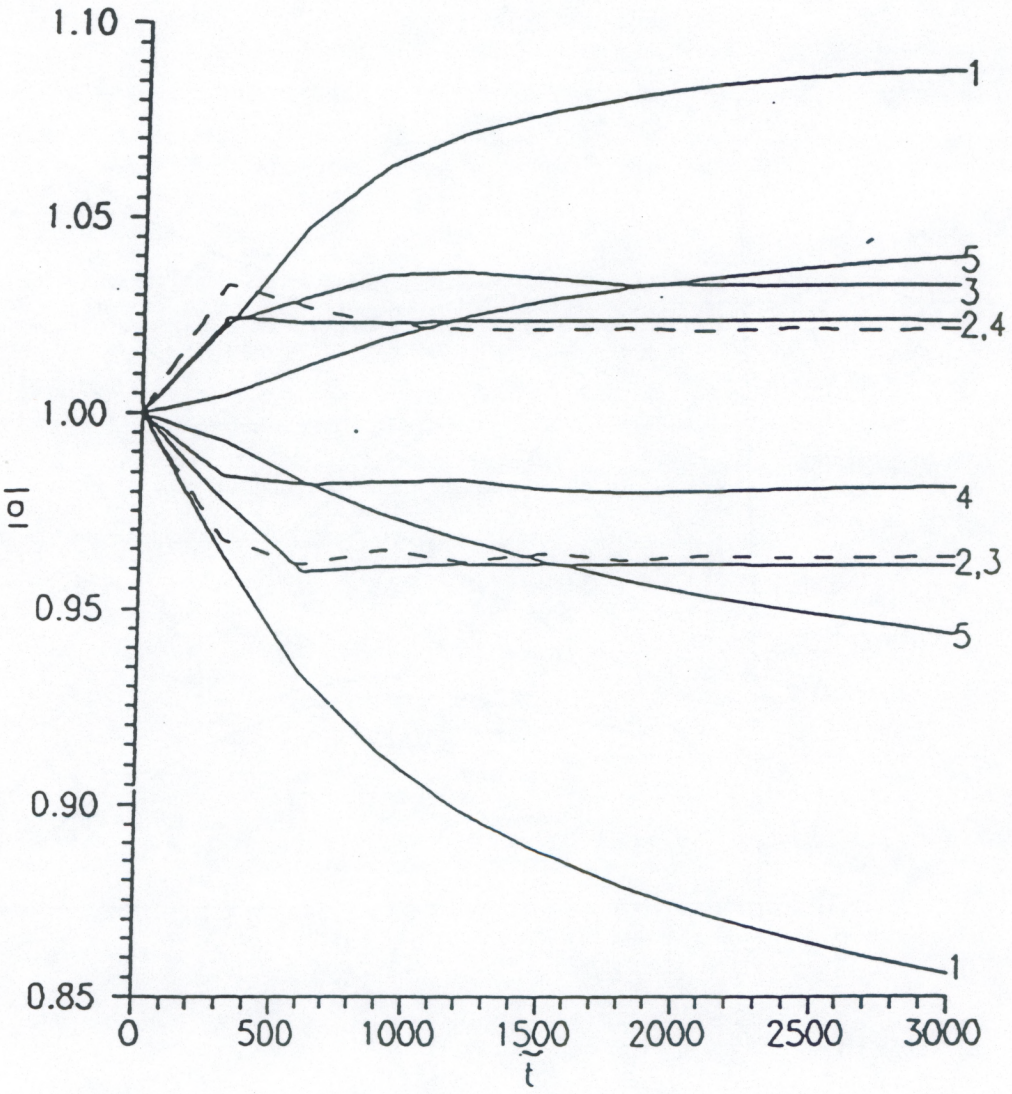

Figure 2. Time variation of maximum and minimum values of modulus of surface wave-field amplitude $|a|$ over entire region of calculations ($c = 2$): 1 - $\tilde{k}_{x0} = 1$, $\tilde{k}_{y0} = 0$, $h = 10$; 2 - $\tilde{k}_{x0} = 1.2$, $\tilde{k}_{y0} = 0$, $h = 10$; 3 - $\tilde{k}_{x0} = 1$, $\tilde{k}_{y0} = 0.2$, $h = 10$; 4 - $\tilde{k}_{x0} = 0.8$, $\tilde{k}_{y0} = 0.2$, $h = 10$; 5 - $\tilde{k}_{x0} = 1$, $\tilde{k}_{y0} = 0$, $h = 20$

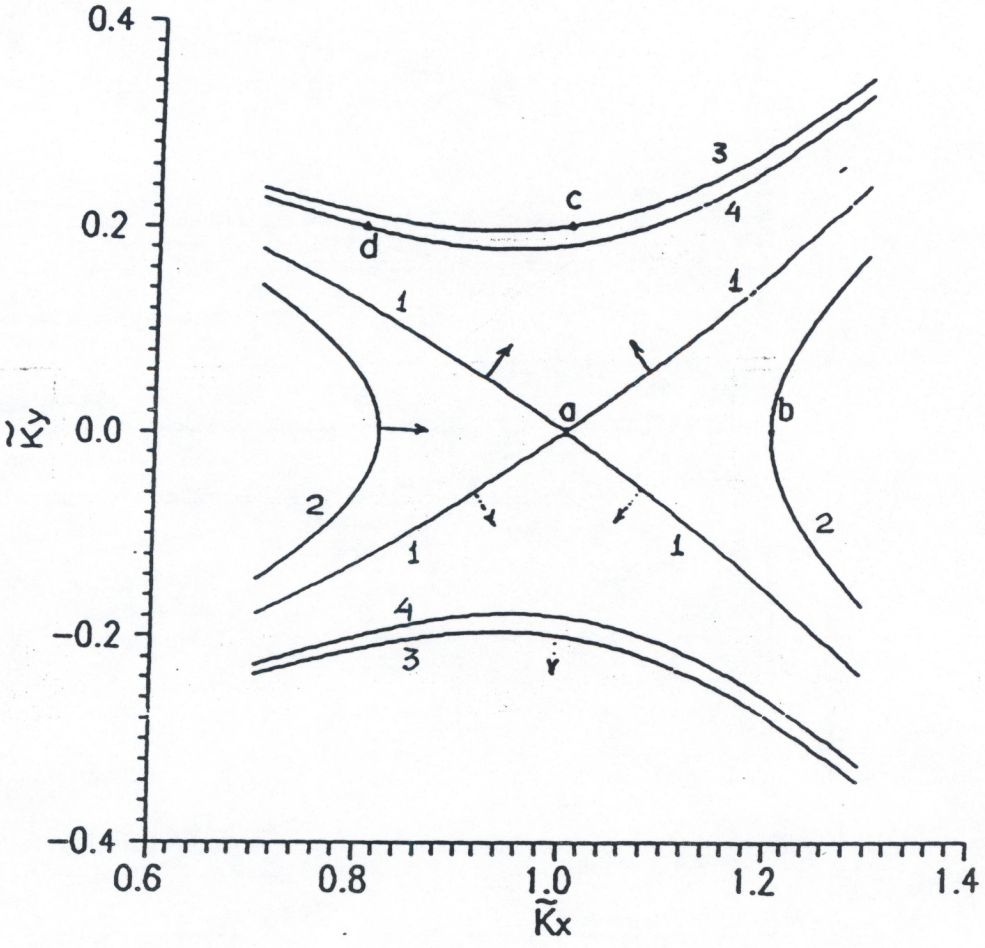

Figure 3. Isofrequencies of surface waves.

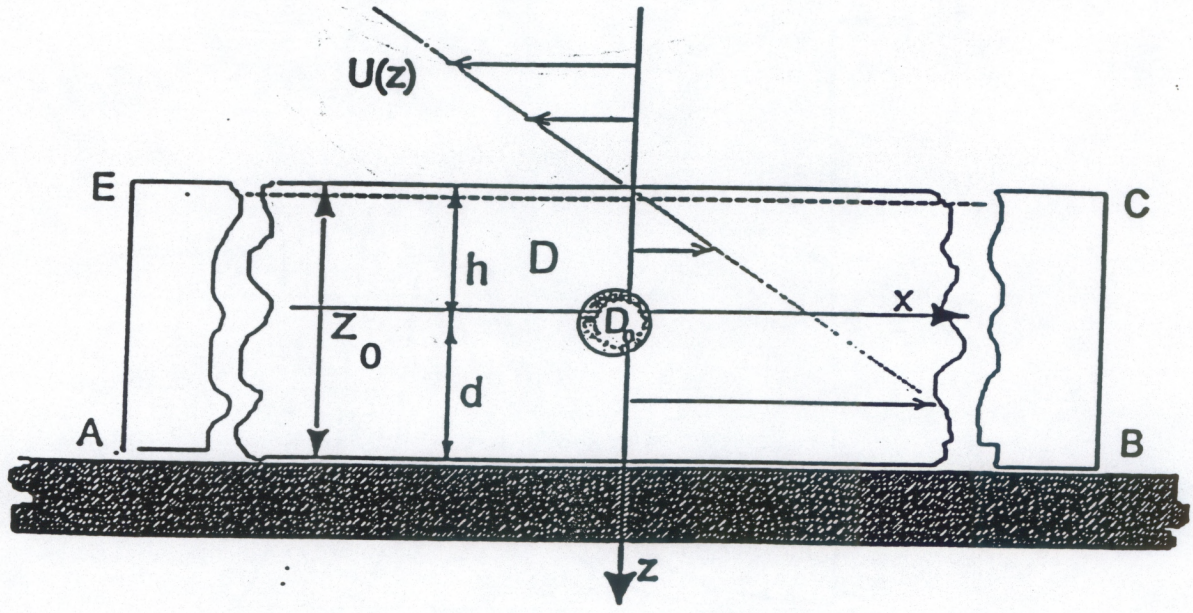

Fig. 4. Geometry of the problem: shear flow around a cylinder

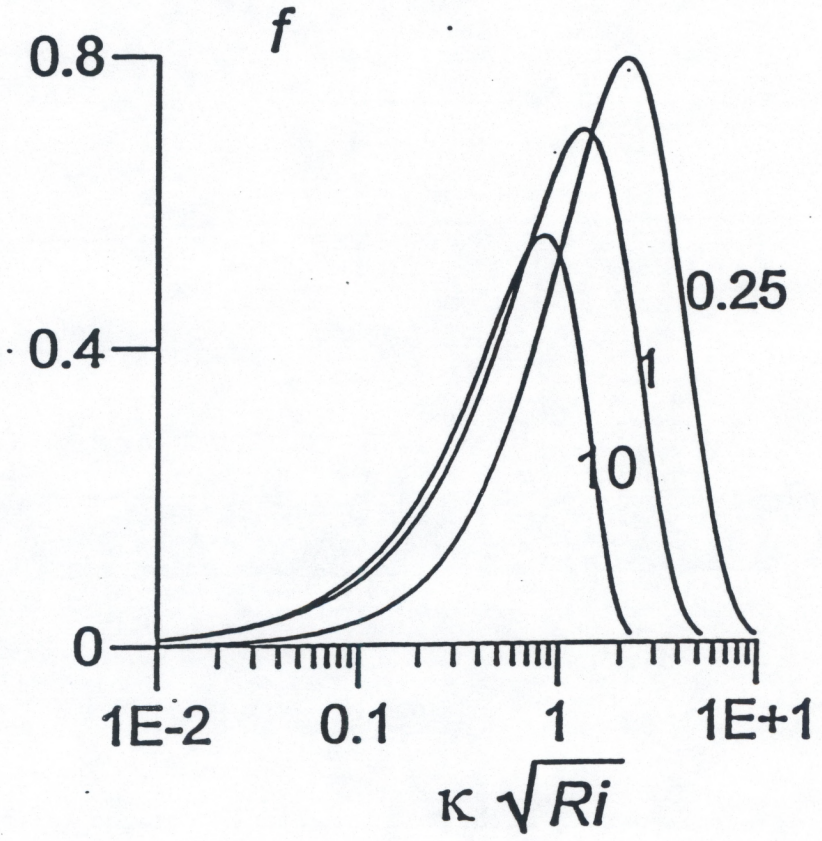

Fig. 5a. Transfer functions. $d/z_0 = 0$, $h > 0$. Near curves = values of Ri numbers.

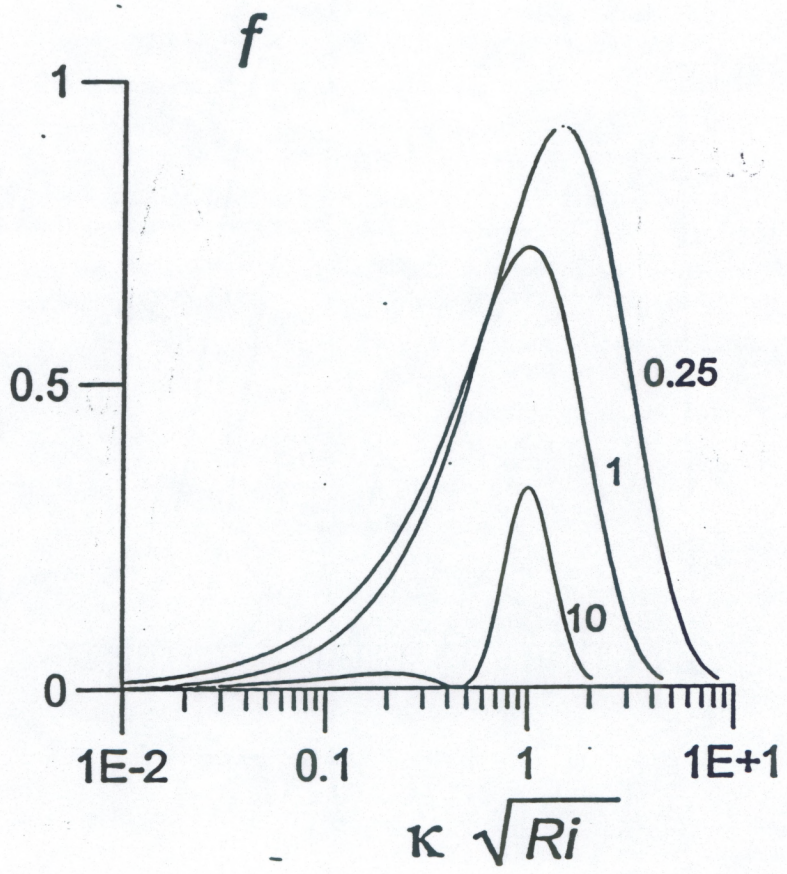

Fig. 5b. Transfer functions. $d/z_0 = 0.5$, $h > 0$. Near curves = values of Ri numbers.

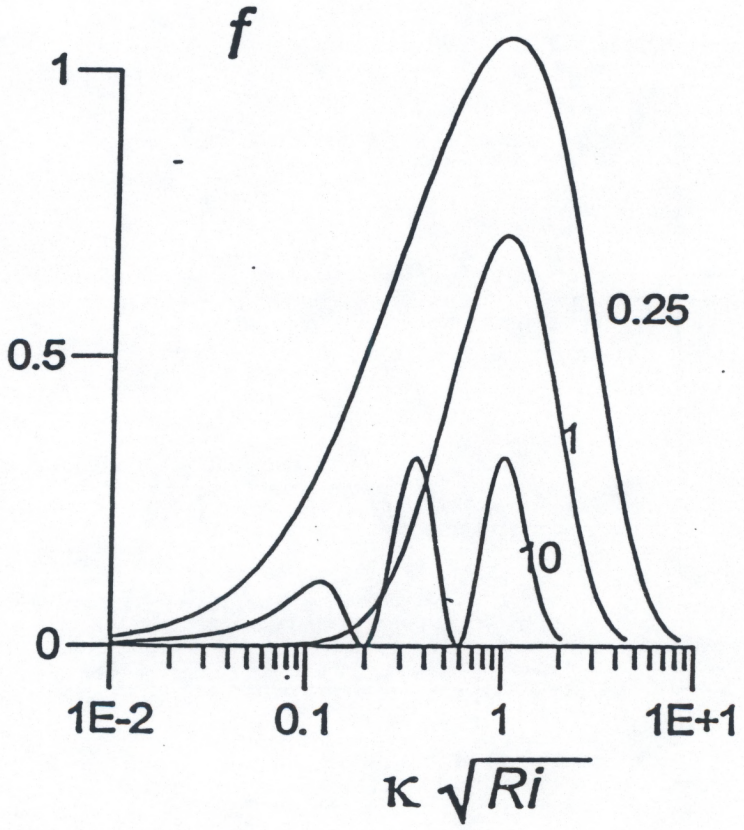

Fig. 5c. Transfer functions. $d/z_0 = 0.9$, $h > 0$. Near curves = values of Ri numbers.

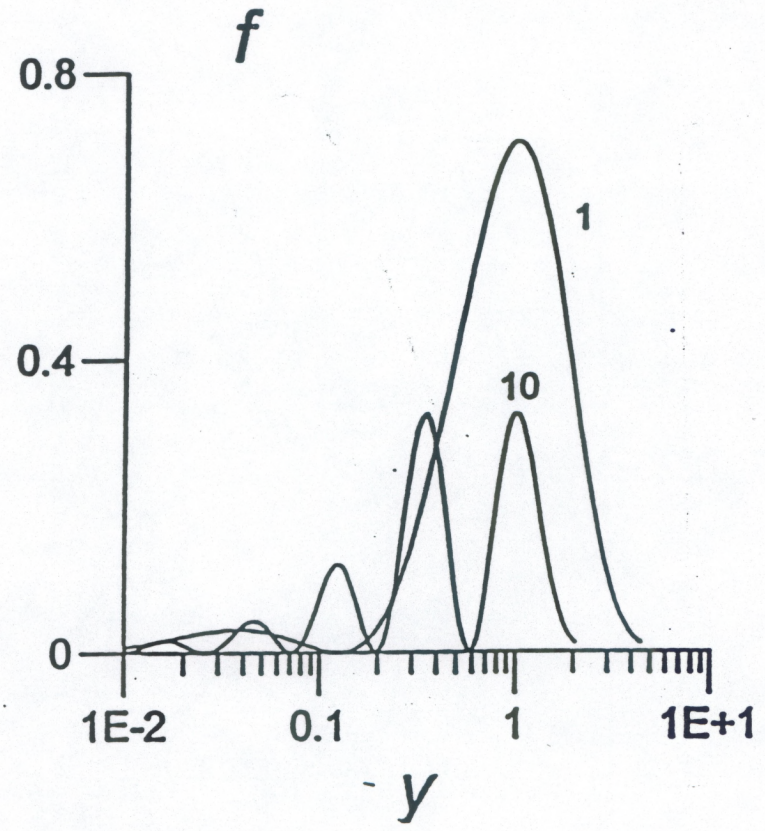

Fig. 5d. Transfer functions. $h < 0$. Near curves = values of Ri numbers.

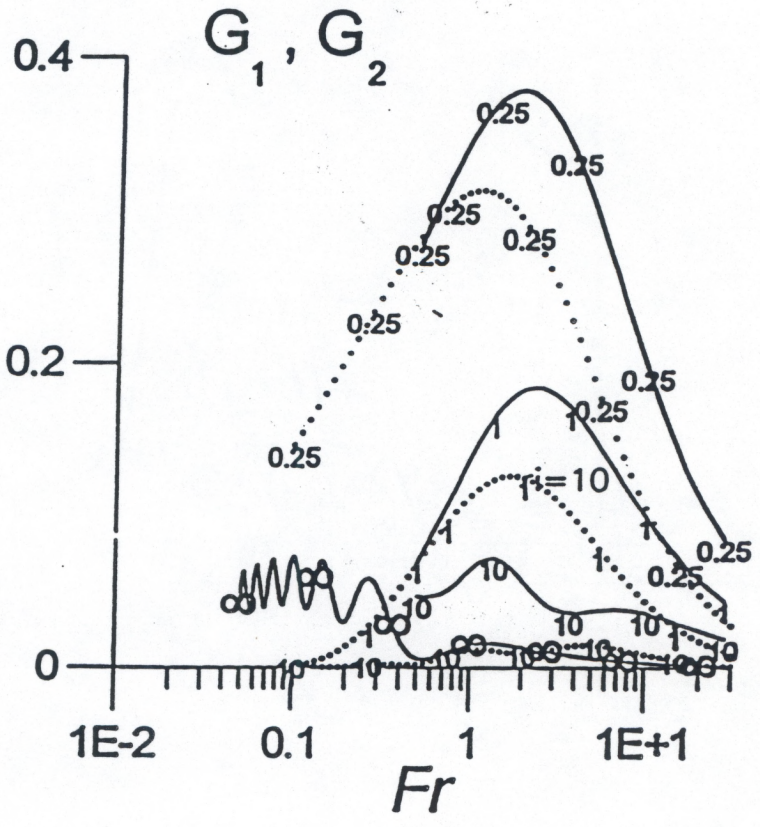

Fig. 6a. Wave drag and "lift force" versus Fr at $a/d = 0.1$, $h > 0$. Solid lines = wave loss, dashed lines = "lift force." Near curves = Ri values.

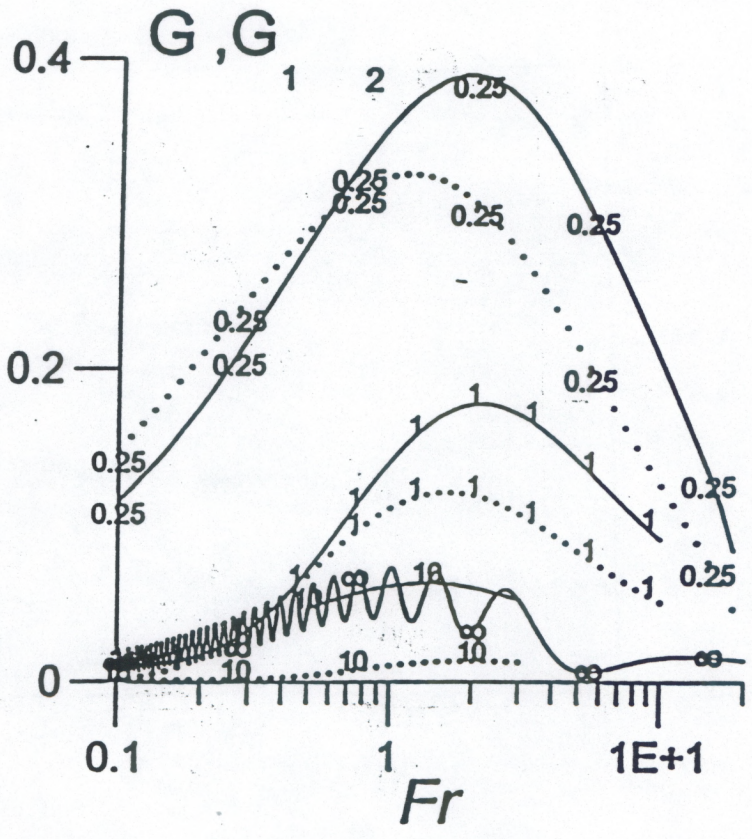

Fig. 6b. Wave drag and "lift force" versus Fr at $a/d = 0.1$, $h < 0$. Solid lines - wave loss, dashed lines = "lift force." Near curves = Ri values.

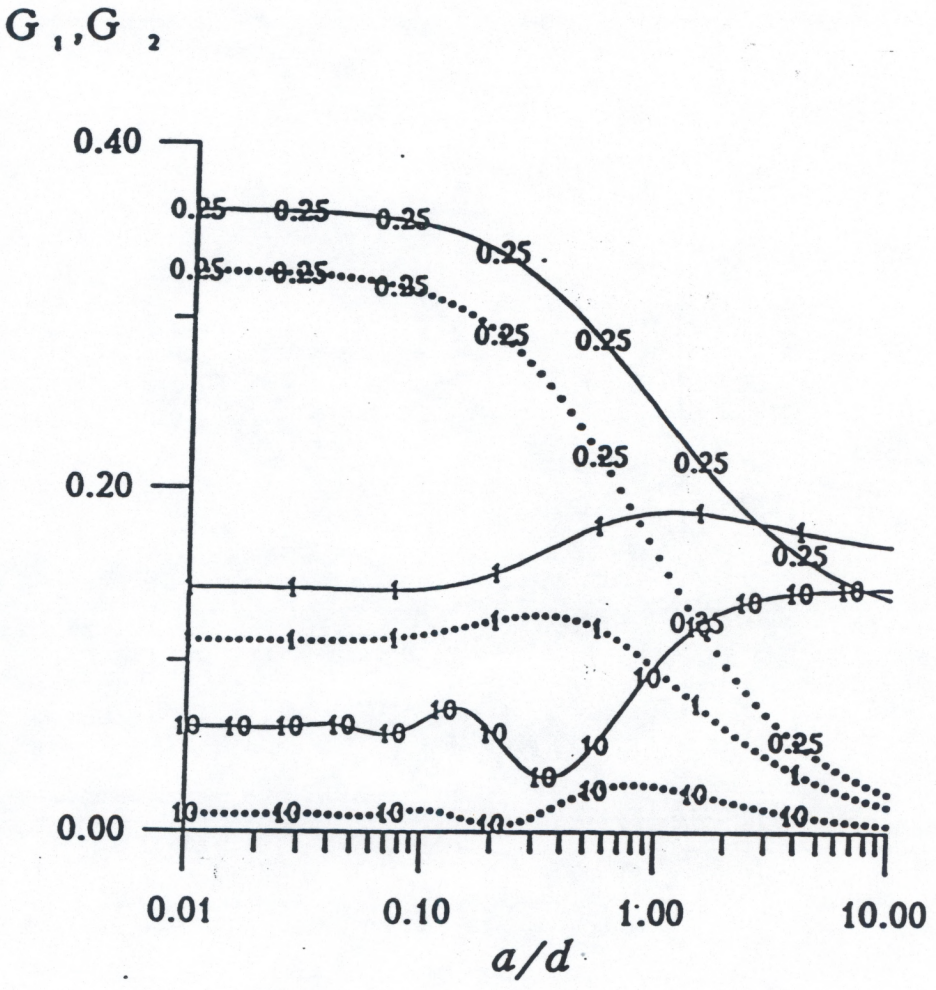

Fig. 6c. Wave drag and "lift force" versus a/d for $Fr = 1$, $h > 0$. Solid lines = wave loss, dashed lines = "lift force." Near curves = Ri values.

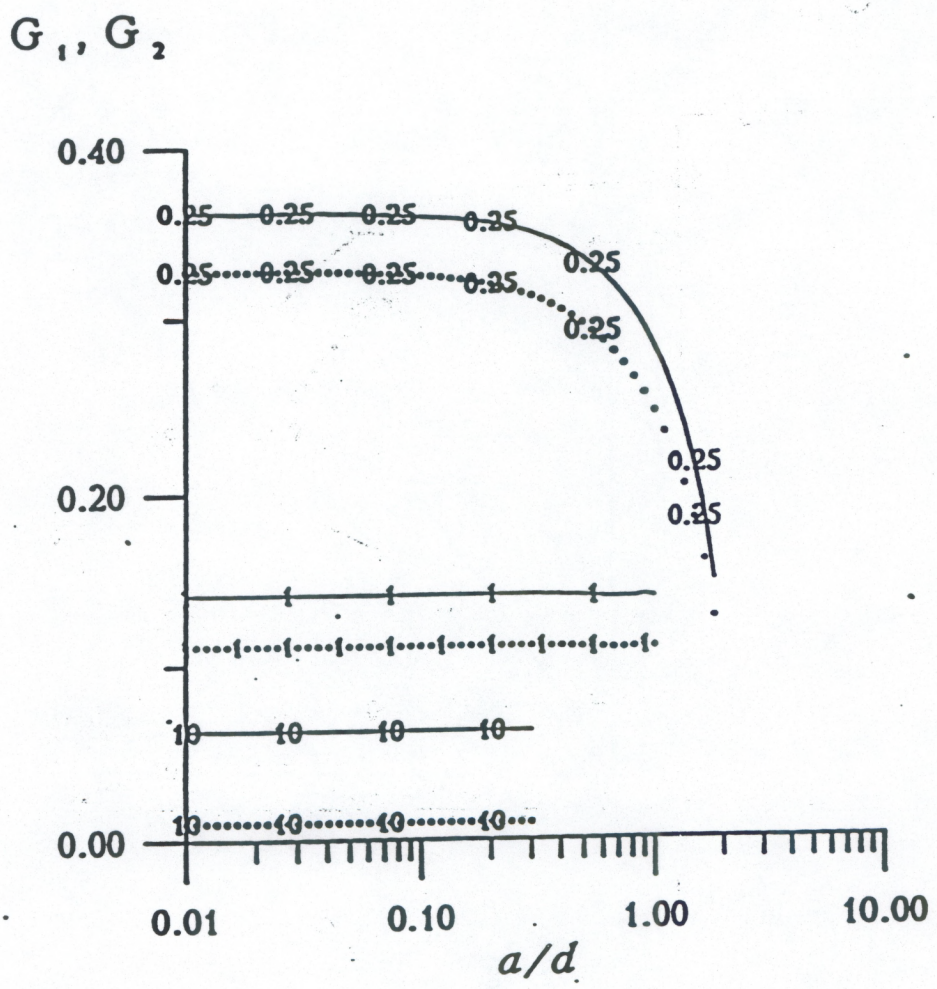

Fig. 6d. Wave drag and "lift force" versus a/d for $Fr = 1$, $h < 0$. Solid lines = wave loss, dashed lines = "lift force". Near curves = Ri values.

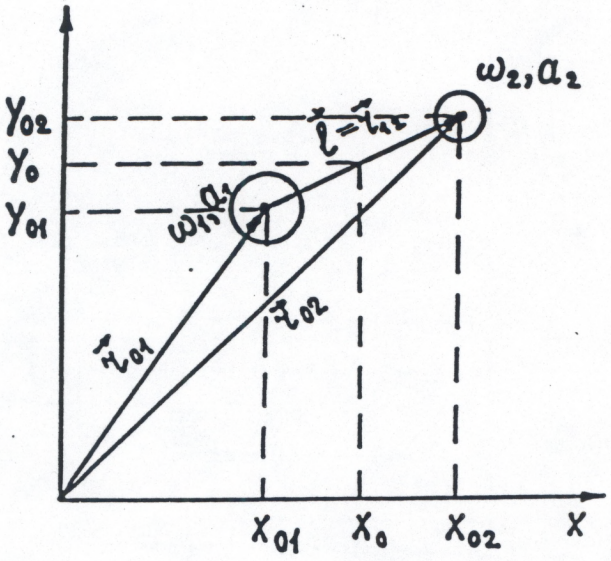

Fig. 7. The vortex pair

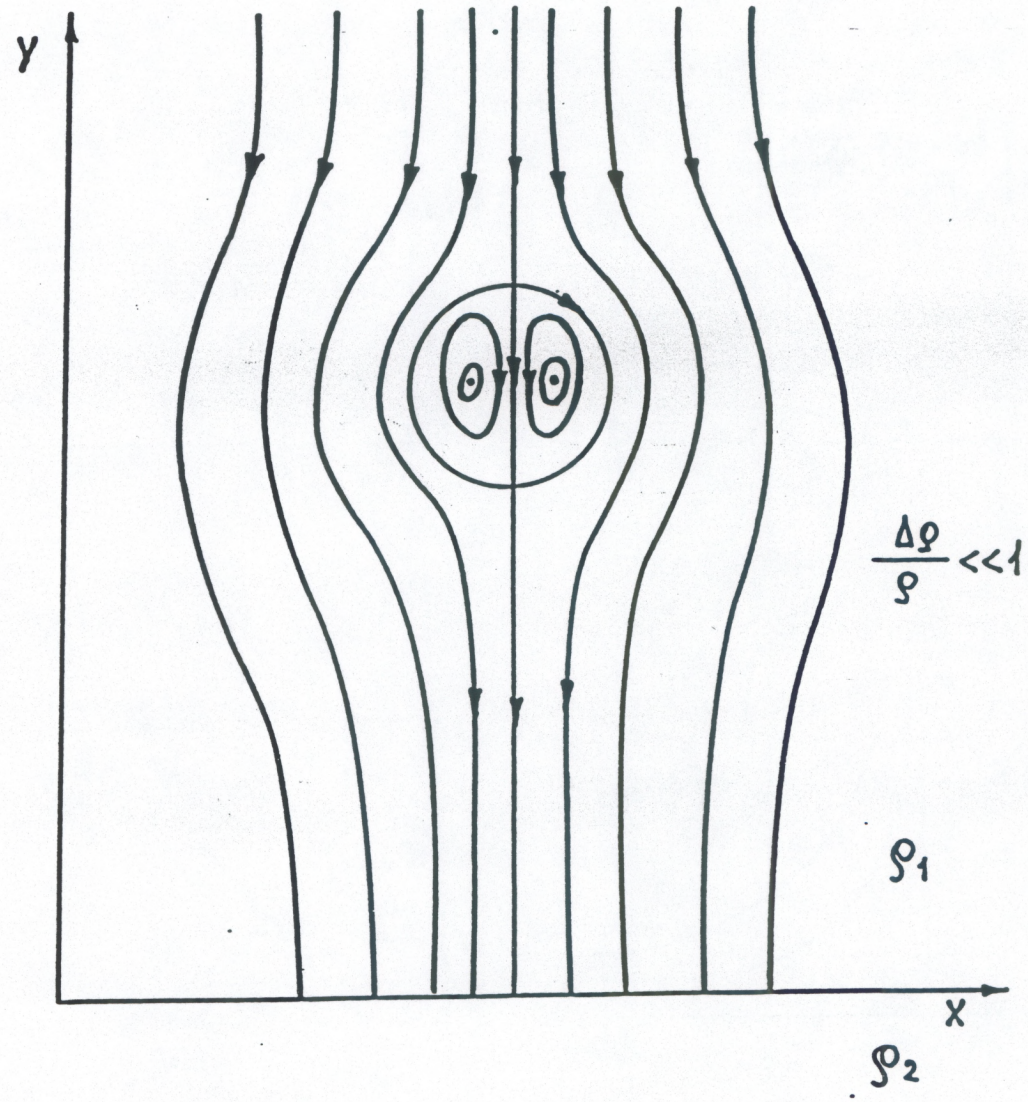

Fig. 8. The velocity field of the vortex pair

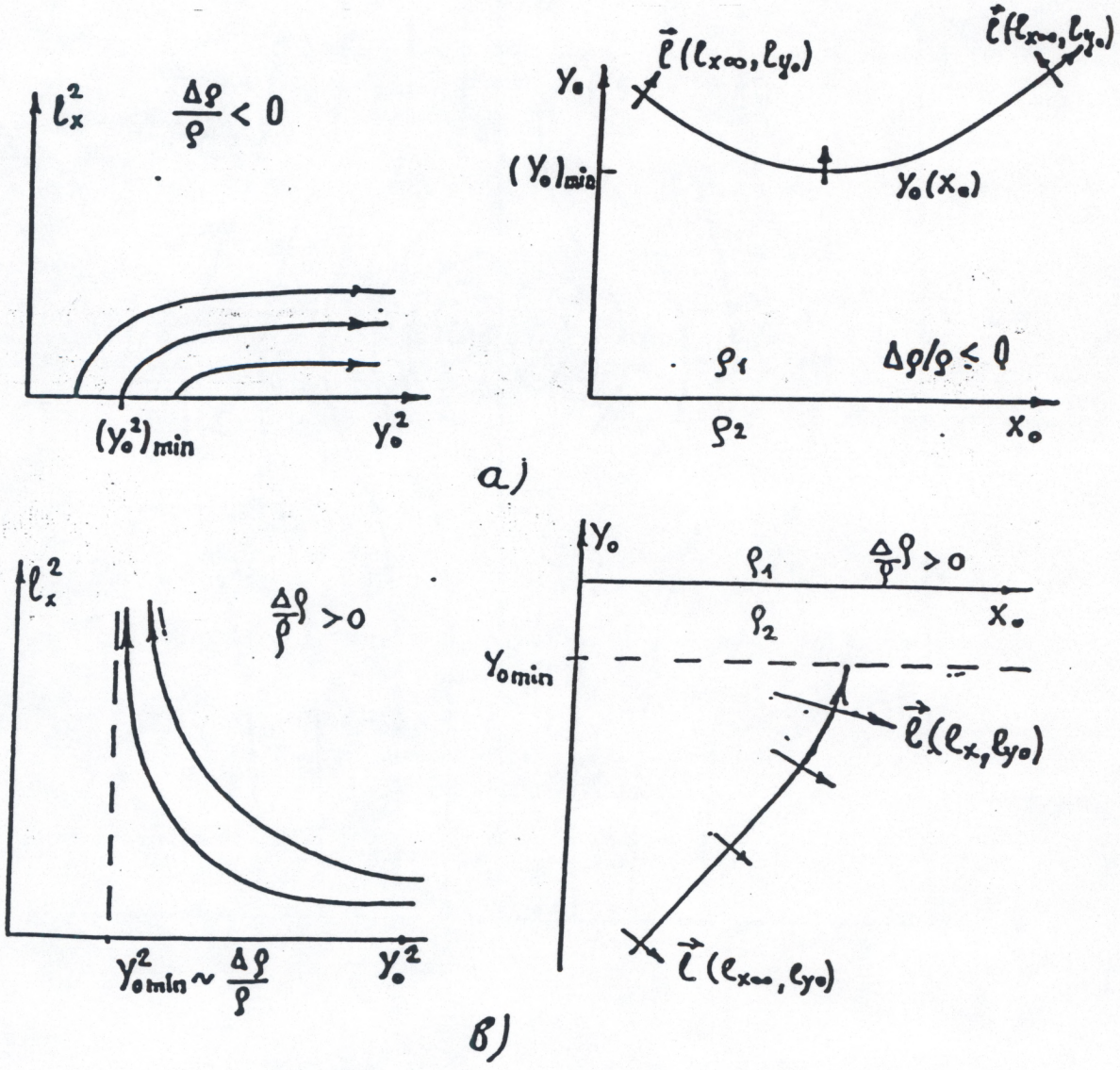

Fig. 9. Type of the $l_x^2(y_0^2)$ dependence and possible type of the motion of the vortex pair at a) $\frac{\Delta\rho}{\rho} < 0$ b) and $\frac{\Delta\rho}{\rho} > 0$.

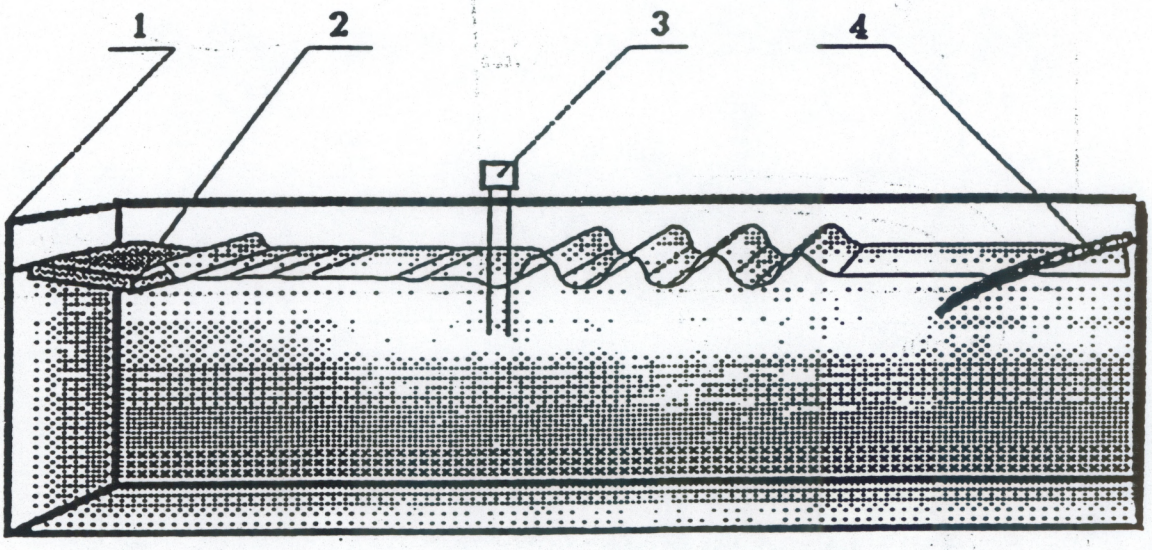

Fig. 10 Scheme of generation of deep—water short intense gravity wave train in the big tank.

1.—big tank (20 x 4 x 2) m ^{3} ; 2.—wavemaker of gravity waves; 3.—sensor of water surface deviations from the equilibrium; 4.—absorber of gravity waves.

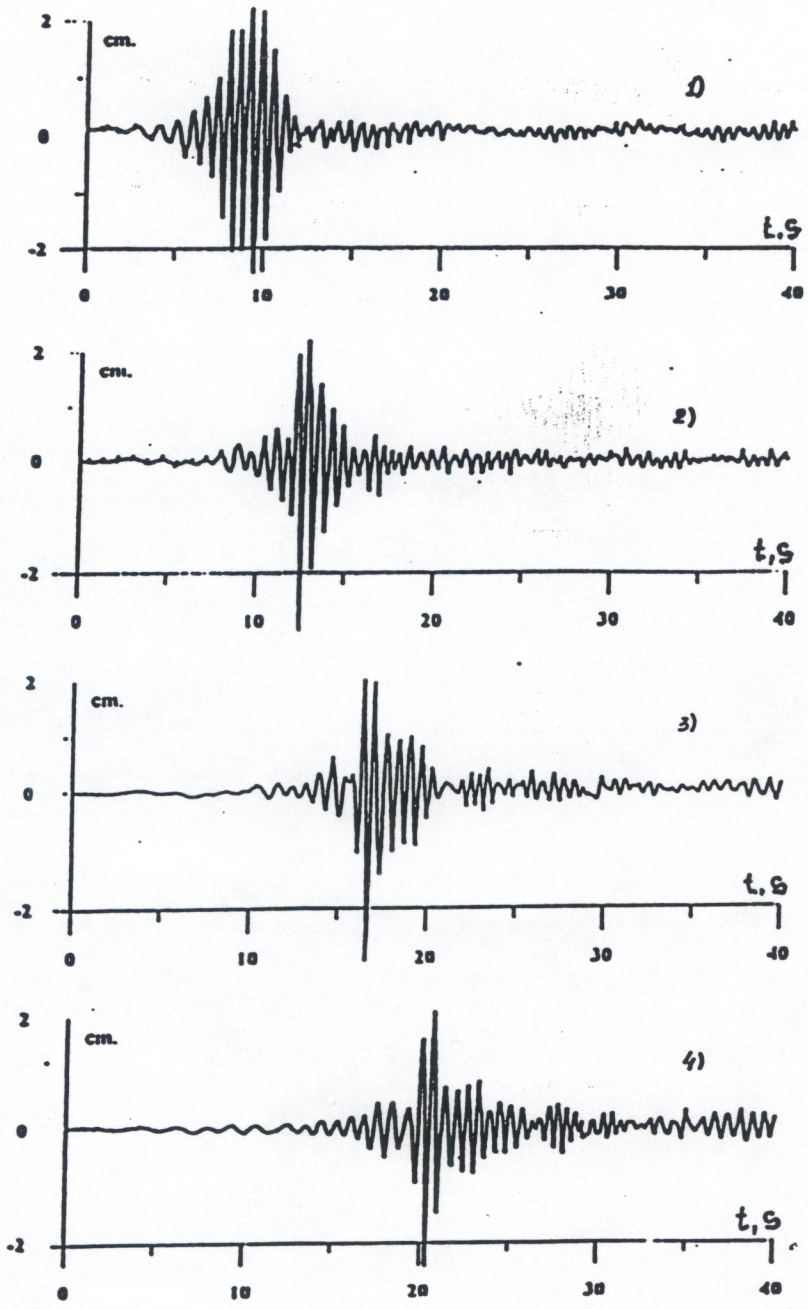

Fig. 11a. The oscillograms of the water surface at different distances L from the wave maker for the initial amplitude $a = 3$ cm: 1) $L = 4$m; 2) $L = 6$ m; 3) L=8m; 4)$L = 10$ m.

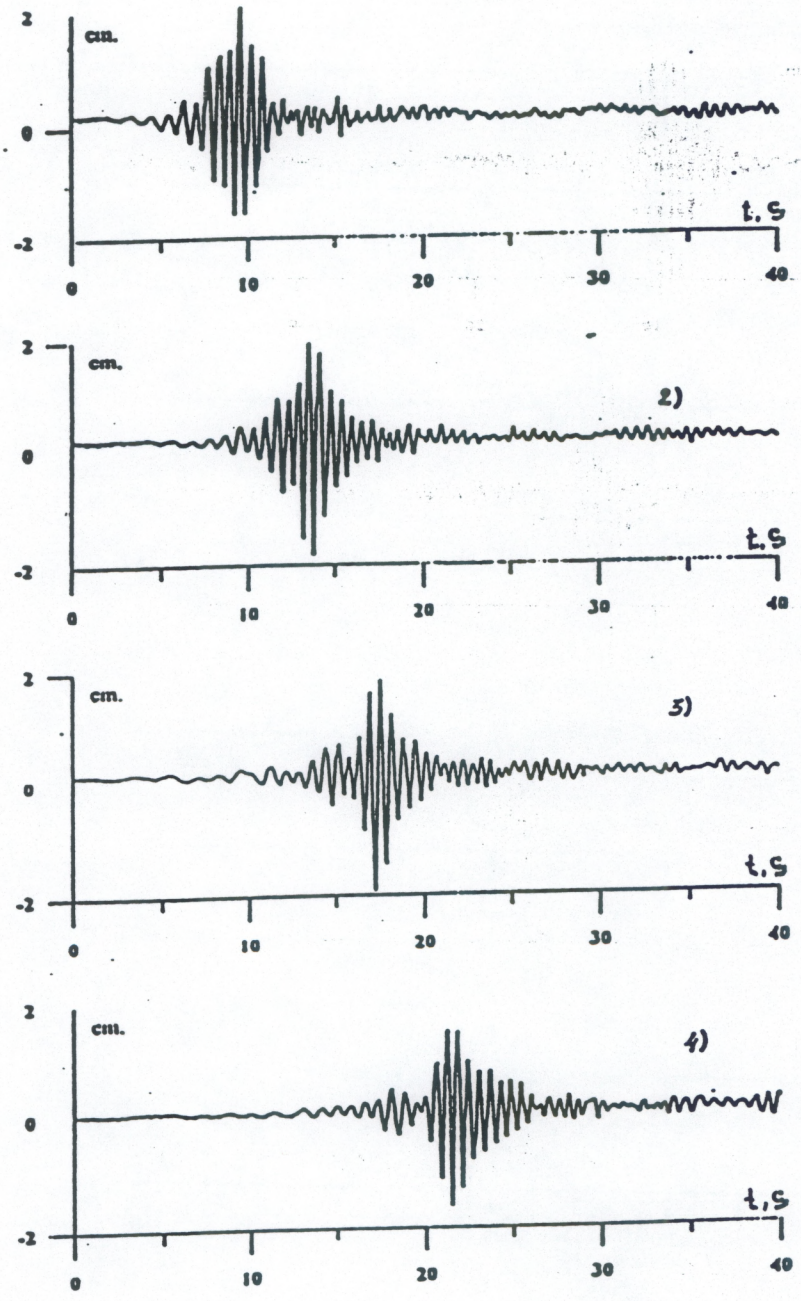

Fig. 11b. The oscillograms of the water surface at different distances L from the wave maker for the initial amplitude $a = 2$ cm: 1) $L = 4$m; 2) $L = 6$ m; 3) L=8m; 4)$L = 10$ m.

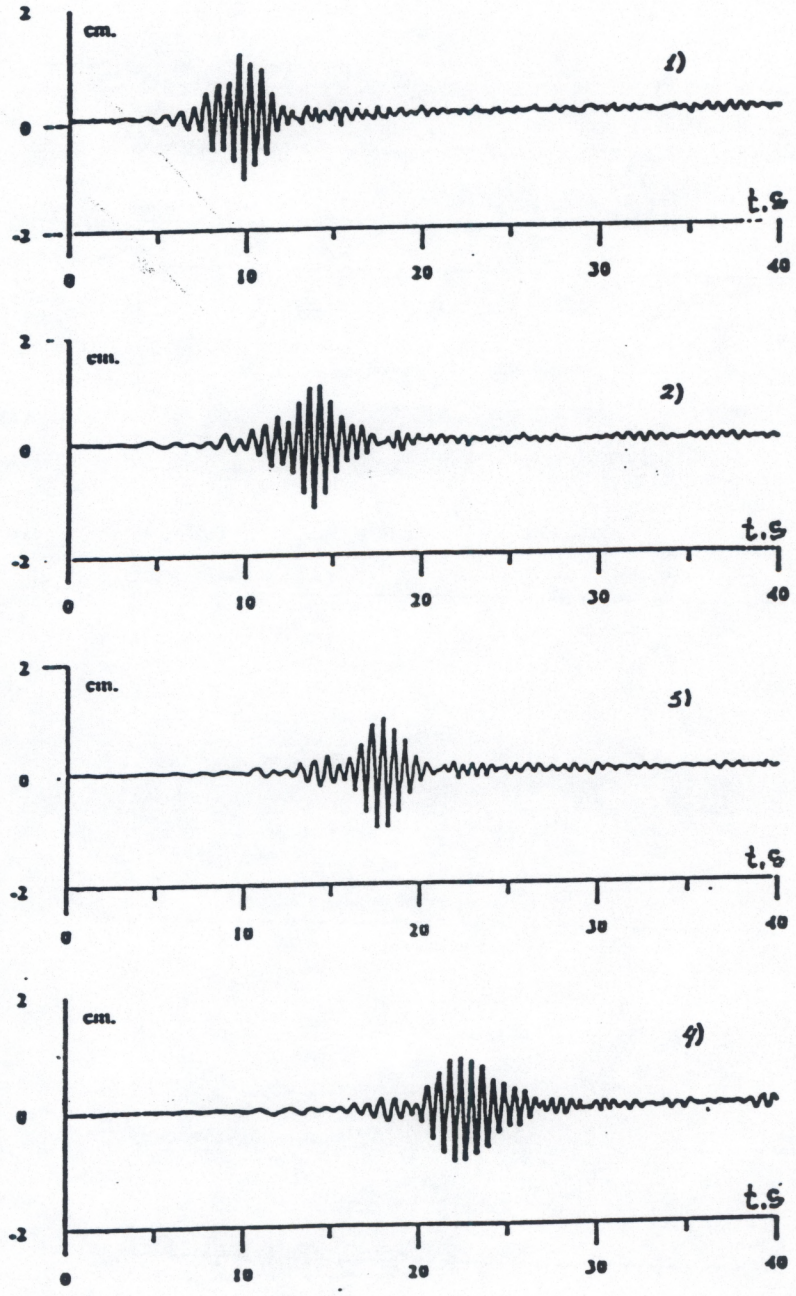

Fig. 11c. The oscillograms of the water surface at different distances L from the wave maker for the initial amplitude $a = 1$ cm: 1) $L = 4$m; 2) $L = 6$ m; 3) L=8m; 4)$L = 10$ m.

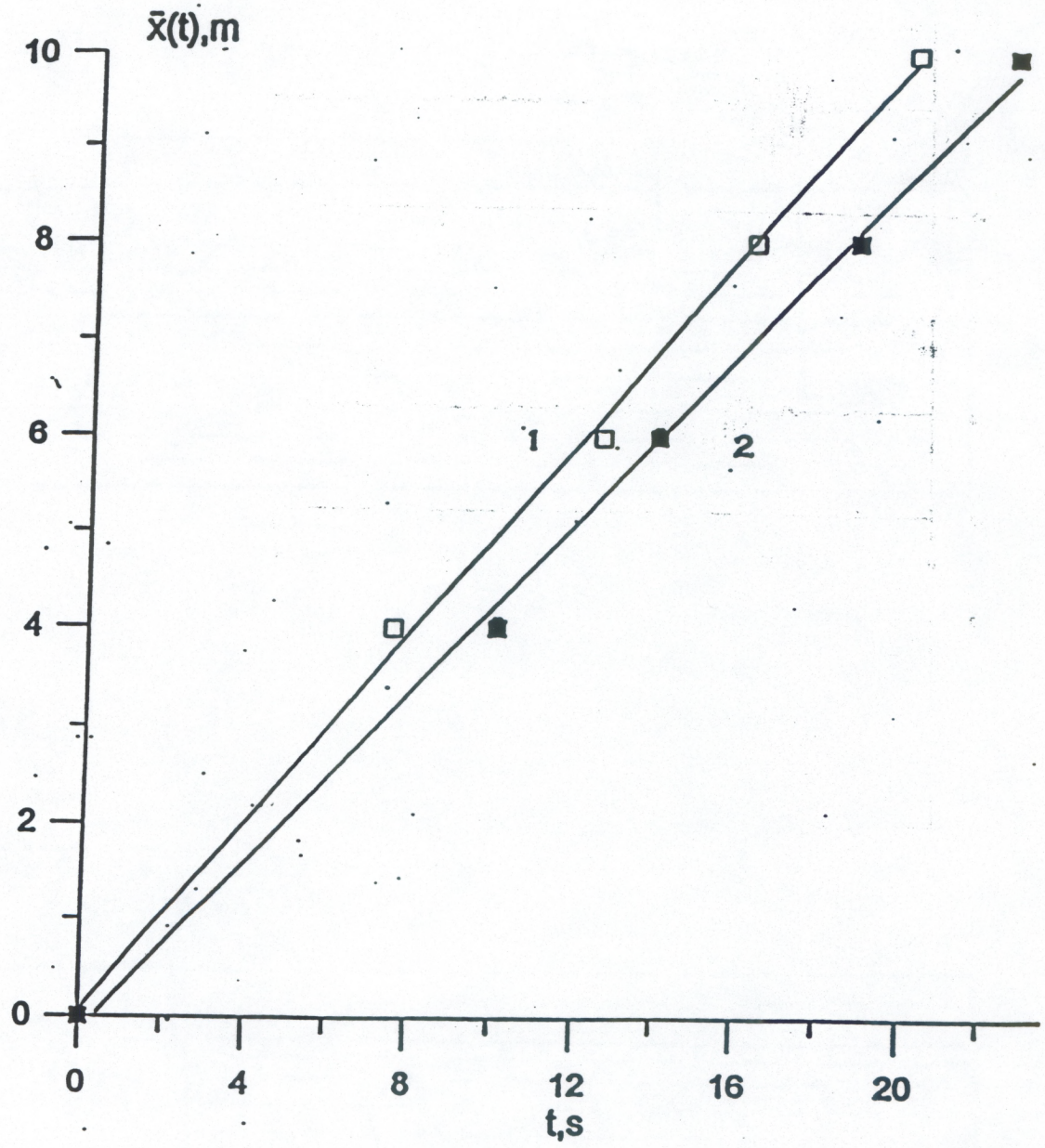

Fig. 12. The dependence of the energy center coordinate $\overline{x(t)}$ of the wave train on time for different values of water surface displacement a = 3cm and 1cm (curves 1 and 2 correspondingly).

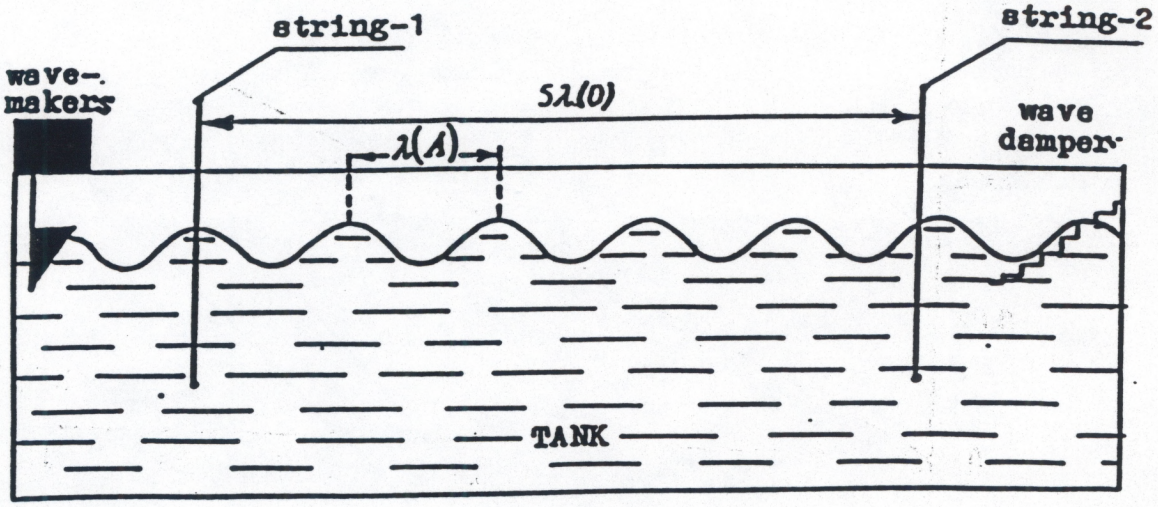

a)

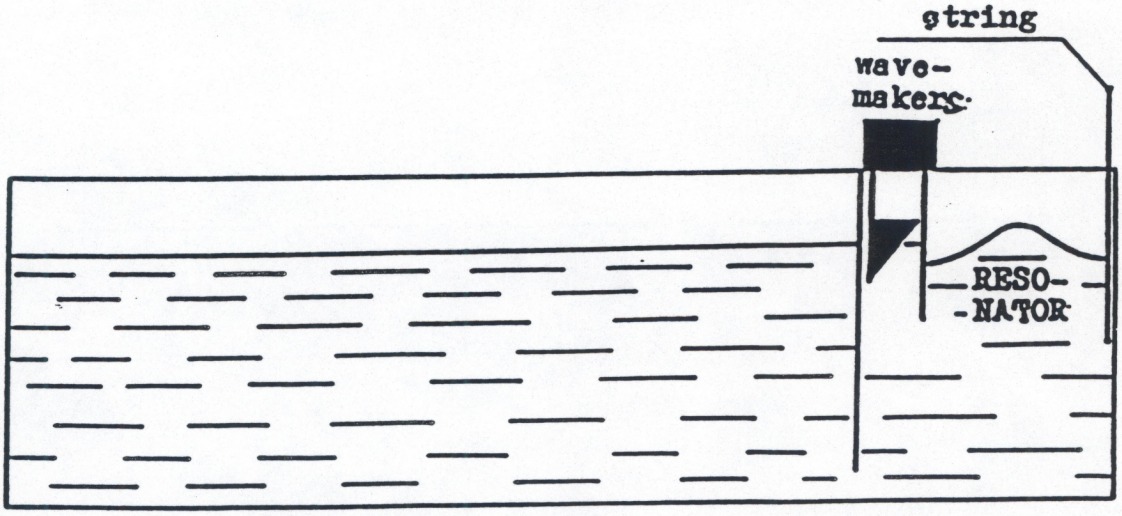

b)

Fig. 13. Experimental setups for measuring nonlinear additions a) to the phase velocity of a travelling wave; b) to the frequency of a standing wave

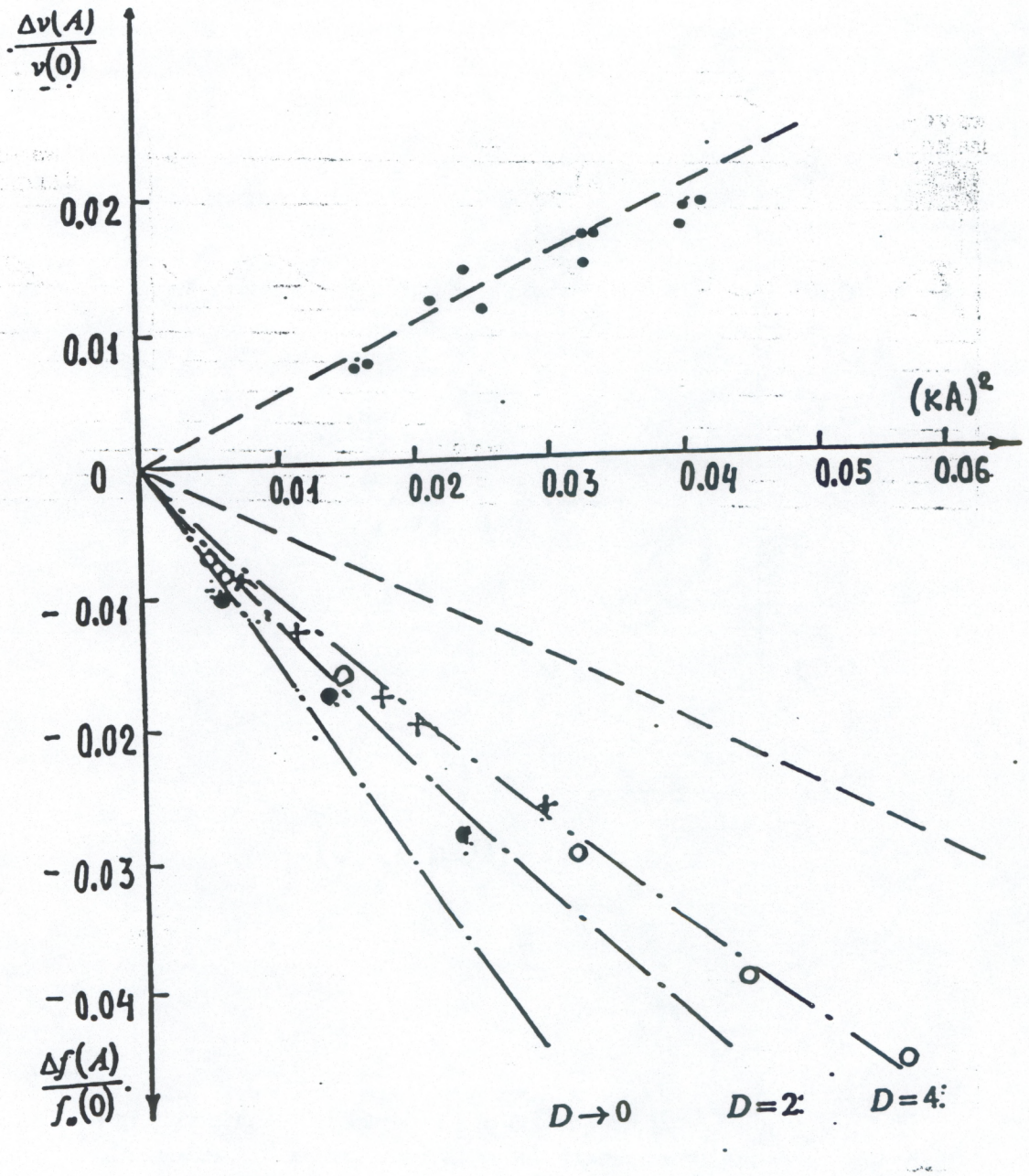

Fig. 14. Relative nonlinear addition to the phase speed of a travelling wave (...) and to the frequency of a standing wave (+++,ooo). Dashed lines correspond to calculation by the formula (36), while the dash-dot line by the formula (45).

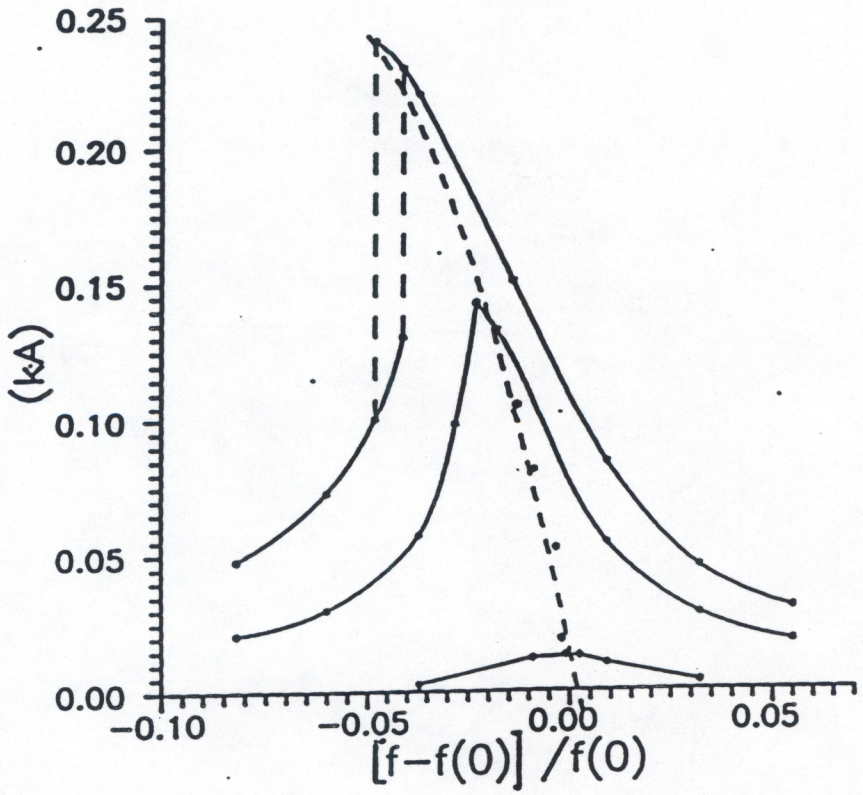

Fig. 15. Steepness kA of the first oscillation mode in a resonator of length $l_0 = 17.1cm$ versus frequency mismatch of the source with respect to the nonlinear resonance frequency $f_0(0)$. The dashed line shows the deviation values of the nonlinear resonance frequency $f_0(kA)$ with respect to the frequency $f_0(0)$ of the linear one.

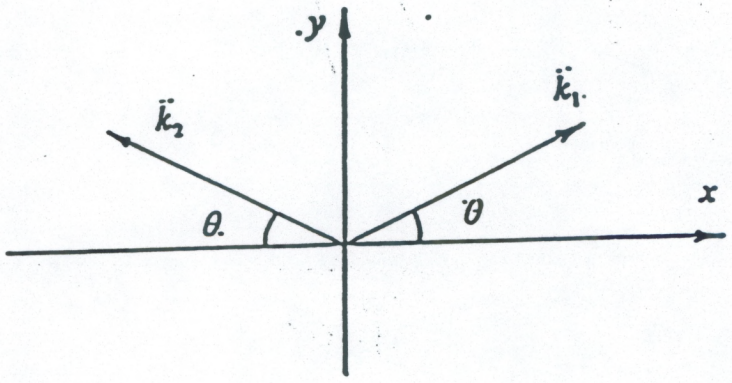

Fig. 16. Orientation of wave vectors $\vec{k}_1$ and $\vec{k}_2$ in the horizontal plane x, y